PROBING THE MECHANICAL PROPERTIES OF GRAPHENE AND GRAPHENE-POLYMER NANOCOMPOSITES USING MOLECULAR DYNAMICS SIMULATIONS

Fatemeh Monji

A Thesis Submitted to The Faculty of Graduate Studies

in Partial Fulfillment of the Requirements for the Degree

of Master of Applied Science

Graduate Program in Mechanical Engineering

York University

Toronto, Ontario

January 2022

© Fatemeh Monji, 2022

Abstract

In the literature, few works have been focused on revealing fundamental mechanisms for the effects of non-bonded interlayer interactions on the mechanical properties of multilayer graphene. To bridge this gap, a series of molecular dynamics simulations was performed in this thesis to provide information from atomistic levels. It was revealed that non-bonded interactions play different roles during tensile stretch and nanoindentation. More importantly, strain analysis suggested that while interlayer interactions have insignificant effects on the distribution of normal strains, they can initiate “strain shielding” for the distribution of shear strains. Hybrids of graphene/boron nitride sheets were then built as demonstrations to further validate these findings. Following this, a set of indentation simulations was performed on graphene/polymer composite to probe the reinforcing role of bi-/tri-layer graphene under different indentation conditions. The results reported in this thesis shed lights on the design of mechanically robust multilayer graphene as well as graphene-reinforced composites.

Acknowledgements

Foremost, I would like to express my sincere gratitude to my supervisor Prof. Cuiying Jian for the continuous support of my master's study and research, for her immense knowledge, motivation, and enthusiasm. Her insightful feedback and advice carried me through all the stages of my studies and research. Besides my supervisor, I would like to thank my thesis committee member, Dr. Garrett Melenka for his insightful comments and practical questions.

I acknowledge the computing resources and technical support from Compute Canada. Also, I would like to thank York University, Department of Mechanical Engineering, and Lassonde School of Engineering for all their support of this research.

And finally, to my one and only Milad who has been my greatest inspiration. I dedicate this thesis to my husband for his love and partnership for success in my life.

Table of Contents

List of Tables

List of Figures

Chapter 1. Introduction

1.1 What is Graphene

Since its first isolation, graphene has drawn wide attentions in different areas of science and technology [1]. Graphene is a 2D matrix of carbon atoms arranged in a honeycomb lattice. Although the existence of graphene was reported by Philip R Wallace in 1947 [2], stable graphene of single-atom-thick crystalline layer was first exfoliated from graphite in 2004. Andre Geim and Kostya Novoselov used a common adhesive tape and exfoliated graphite into just a few layers of graphene [3]. Graphene is the basic building block for many other materials in different dimensions. Figure 1.1 shows three different materials that can be formed from graphene. As can be seen, the flat monolayer of carbon atoms could be swaddled into fullerene, rolled into nanotubes (CNT), and stacked into 3D graphite [4]. Typically, graphene refers to nanosheets with a thickness less than 100 nanometers [5].

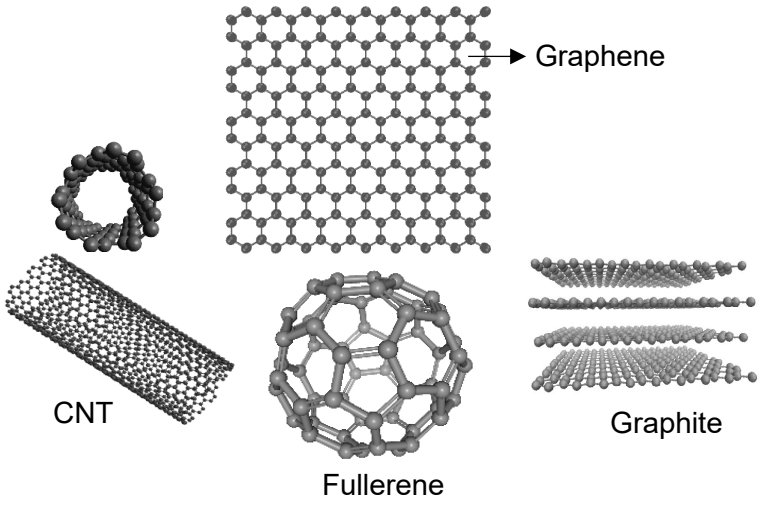

Figure 1.1 Graphene as the fundamental structure for many other carbon materials

In graphene, each atom is connected to three other carbon atoms. However, carbon atoms have a total of 6 electrons with 2 in the inner shell and 4 in the outer shell. The bonding formed in graphene thus leaves one electron out in the third dimension. These electrons are highly-mobile, and located above and below the graphene layer [6]. Due to its special bonding, graphene has superior electronic, mechanical, and thermal properties [1]. Also, graphene is inhomogeneous, and its properties can be dependent on chirality, i.e., directions, (see section 3.1 for more details) [7]. Given the wide applications of graphene as reinforcement material, this thesis focuses on the mechanical properties of graphene.

1.3 Mechanical Properties of Graphene

In general, measurements of the mechanical properties of graphene can be performed by using a series of theoretical and experimental approaches. From experimental perspectives, tensile and nanoindentation tests on graphene can be performed by using Atomic Force Microscopy (AFM), Scanning Electron Microscopy (SEM), or Raman spectroscopy setups. On the other hand, numerical analysis such as molecular dynamics (MD), density functional theory (DFT), and finite element method (FEM) have also been widely used for studying the mechanical properties of graphene [5, 8, 9].

AFM is widely used for probing the nanoindentation behavior of 2D materials such as graphene [10]. In this technique, a hard indenter tip with known mechanical properties presses against the sample surface until the surface is deformed by the indenter. The local mechanical properties can then be obtained by analyzing the relationship between the applied force and the sample deformation [11]. In SEM, a high

energy beam of electrons is focused on a sample surface. This results in several types of interactions such as backscattered electrons, X-rays, diffraction patterns, and so on, which can be used to analyze the mechanical properties in SEM. Raman spectroscopy is based upon the light interaction with the chemical bonds within the materials, and the results in this method can provide information on chemical structure, phase and crystallinity, and molecular interactions [12]. MD, DFT, and FEM are computational tools for measuring mechanical properties [13]. FEM analysis is not applicable in nanoscale [14]; DFT method is computationally expensive and suitable for systems with small number of atoms [15]. MD simulation method (more details in chapter 2) on the other hand is cost effective and can be used for analysis at nanoscale [16].

In 2008, Lee and co-workers [17] measured the elastic properties and intrinsic breaking strength of free-standing monolayer graphene membranes by performing nanoindentation tests using AFM. They discovered that graphene is the strongest material ever measured with brittle fracture and non-linear elasticity. The Young's modulus was reported to be $E = 1.0 \pm 0.1\ \mathrm{TPa}$, where E is the Young's moduli obtained from the slope of the linear part in the stress-strain plot. Although the mechanical strength of graphene was reported to be close to 42 Nm^{-1} (equivalent to 130 GPa) [18–21], tearing a sheet of graphene is as easy as tearing a paper. The reason for this behavior is due to the presence of defects. Zandiatashbar et al. [22] showed that the elastic modulus and strength of graphene are not sensitive to sp^3-type defects, but largely dependent on vacancy defects. The sp^3-type defects are formed as a result of the presence of three electrons in the outer shell of carbon atoms, different from the ground state where carbon atoms have two unpaired electrons in their outer shell.

Another reason for the aforementioned behavior is due to the weak interlayer interactions among graphene. Han et al., [23] studied the effect of boundary conditions on the elastic modulus using MD simulations. It was shown that when graphene was fully clamped, a constant elastic modulus was obtained, regardless of the number of graphene layers. However, when graphene was weakly clamped, i.e., weakly fixed, interlayer sliding was present, leading to imperfect stacking. Furthermore, the elastic modulus was decreased by increasing the number of graphene layers. In the work of Li et al., [24] the interlayer shear resistance of graphene/graphene microstructures was compared with those of boron nitride/boron nitride and graphene/boron nitride through friction tests in MD simulations. According to their results [24], graphene/graphene microstructures have the lowest shear resistance. Thus, a detailed study on the role of interlayer interactions is presented in chapter 3.

1.4 Polymer/Graphene Nanocomposites

Combining various materials with different natures but complementary properties is one of the most promising approaches for preparation of multifunctional materials [25]. Polymer materials, due to their low weight and cost effectiveness, have been widely used in industrial applications. According to the role of mixtures, incorporating graphene as a 2D reinforcement into polymer matrix can result in improvements in strength and toughness of the composite. Graphene/polymer composites are lightweight, strong materials, and have been used for making medical equipment, aircrafts, plastic containers, and much more. Therefore, to ensure mechanical stabilities, studying the mechanical properties of graphene/polymer nanocomposites is important and necessary.

In general, composites are made up of three main parts: reinforcement, matrix, and interface. Graphene and polymer matrix are not chemically bonded, leading to the lack of strong interfacial interaction and an imperfect load transfer between graphene and polymer. Young et al. [26] probed the shear distribution in a model composite consisting of graphene/poly(methyl methacrylate) using Raman Spectroscopy. Their results revealed that at matrix strain up to 0.6%, there is a good stress transfer between graphene and polymer. However, at higher strains, matrix fragmentation takes place, indicating poor adhesion at the interface. Also using Raman Spectroscopy, Gong et al. [27] studied the effects of filler thickness on stress transfer between internal graphene layers within polymer-based nanocomposites. They showed that there is a good stress transfer between monolayer/double-layer graphene and polymer matrix. Furthermore, no slippage was found between graphene layers in double-layer graphene. However, due to interlayer slippage in three-layer/many-layer graphene, an inefficient stress transfer was observed, and the Young's modulus of the polymer nanocomposite was negatively affected by the lack of robustness between graphene reinforcement layers. This interlayer slippage further motivates the study of interlayer interactions in chapter 3, as well as probing the reinforcing role of graphene in polymer composites (chapter 4). In the following section, a brief review of production methods is provided for graphene, as well as graphene-polymer composites.

1.5 Production of Graphene and Graphene-Based Composites

There are two types of classifications for differentiating preparation methods of graphene. Based on the first classification, 2D materials, including graphene, can be prepared by top-down exfoliation in solution, or bottom up synthesis [28]. According to

the second classification that includes a more detailed assortment, preparation of multi-layer and monolayer graphene could be achieved either through direct or indirect methods (summarized in Figure 1.2) [1, 5]. The most common methods for the direct fabrication of graphene include CVD, epitaxial growth on SiC, exfoliation and reduction from graphene oxide. CVD is mainly used in laboratory, and in CVD the heated-up substrate, on which graphene grows, is put in a chamber with constant flow of H_2 at high temperature to reduce the residue air. Then, CH_4 and H_2 is pumped over the substrate for a limited time. Following this, graphene can be formed on the substrate. Regarding the epitaxial growth on SiC, this method is based on sublimation of SiC, through which the graphene growth happens by heating up the SiC wafer with zero pressure and at elevated temperature. Then the silicon atoms will be evaporated, and a thin layer of carbon atoms will be left. As for the mechanical exfoliation, mechanical peeling takes place to break the weak van der Waals forces between the adjacent layers of graphene. The mechanical force can be provided by ultrasonic, an adhesive tape, and some other methods [5]. Compared to direct methods, indirect methods are to produce reduced graphene oxide (rGO) which is the commercial substitute of graphene. The most common technique to synthesis GO was proposed by Hummers et al. [29] This method involves adding graphite and water to the mixture of H_2SO_4-$NaNO_3$-$KMnO_4$. After a set of dilution, separation, drying, washing, and dispersion, graphite oxide (multilayer graphene oxide) solution will be formed. To synthesis graphene oxide from graphite oxide, more exfoliation is demanded [5].

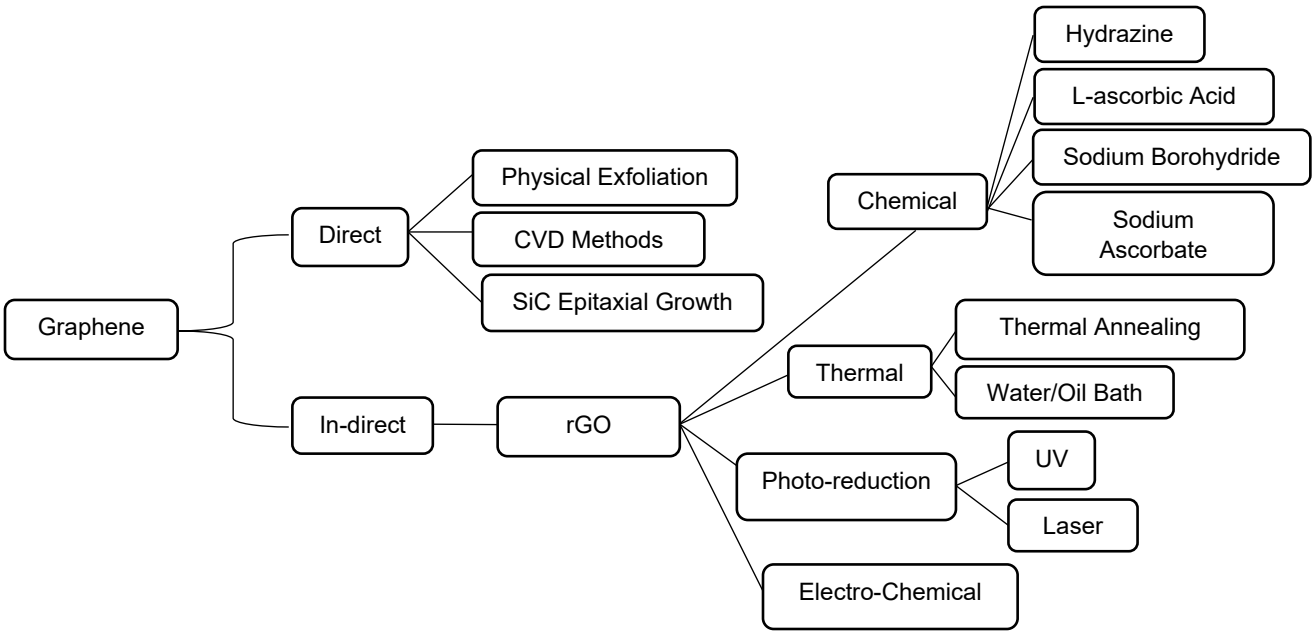

Figure 1.2 Preparation methods of graphene family of materials [5]

Based on rGO, the following methods are commonly used for producing graphene-filled polymer composites: coating, casting, solution mixing, melt blending, and in-situ polymerization. Among these methods, in-situ polymerization, solution processing, and melt-blending have attracted great attentions [30]. In-situ polymerization and solution processing methods are well known for the creation of uniform distributions of graphene in the polymer matrix, and are suitable for producing the composite samples studied in chapter 4 of this thesis. In-situ polymerization method is based on mixing rGO with monomers, and subsequent polymerizing the monomers. In solution processing method, by using sonication mixing methods, rGO dispersed in a solvent is mixed with the polymer solution. Following solvent vaporization, composites are obtained [30]. Melt blending method is mainly used for fabricating thermoplastic polymers. Because of its cost efficiency and ecological nature, melt blending method has been used for mass production of polymer nanocomposites. The disadvantage of

this method is that it may cause graphene shortening, buckling, or rolling, due to using strong shear forces during the fabrication process [30].

1.6 Objectives

This thesis aims to fundamentally elucidate the role of interlayer interactions on the mechanical properties of multilayer graphene during different mechanical testing. Furthermore, it aims to guide the design of mechanically robust nanostructures. To achieve this, the reinforcing role of graphene in composites will also be clarified under different loading conditions. Polyethylene (PE) is chosen in this thesis as the matrix for composites, given its wide applications in food packaging, automotive components, medical products, etc. To provide atomistic insights, molecular dynamics techniques are chosen as the primary approach. The remainder of this thesis is organized as follows: molecular dynamics simulation methods are introduced in section 2, the roles played by interlayer interactions are presented in section 3 (results published in the Journal of Materials Science), investigations on graphene reinforced polyethylene nanocomposites is discussed in chapter 4, and final conclusions, as well as future works, are given in section 5.

Chapter 2. Molecular Dynamics Simulation

In this chapter, an overview is provided for molecular dynamics (MD) techniques.

2.1 Strengths and Advantages of Computational Approaches

Computations and experiments are tightly bounded and essential tools in every scientific work. These two methods are interrelated, and have different strengths and application areas [31]. Specifically, in submicron scales where the mechanical analysis of materials is hardly accessible or impossible by experiments, computational approaches are still applicable as a bridge between theory and experiment [32]. In addition, computational methods are more cost effective and can verify empirical results. Computational methods for studying the structural evolution at the atomic level fall into three broad groups, ab initio, density functional theory (DFT), and MD. Among these methods, ab initio and DFT are based on the Schrodinger equation, and suitable for small systems (i.e., ~3500 atoms, maximum in the current literature) [33], and are computationally expensive. On the other hand, MD method based on “force filed (potential, details in the following sections)” can model systems with a much larger size (e.g., with machine learning, up to ~100 million atoms) [34], and thus is chosen for this thesis.

2.2 MD Method

MD simulation was first used by Alder and Wainwright in 1957 to predict the phase transformation behavior in a hard-sphere system [35]. In general, through pre-defined interaction functions, MD can calculate forces on each particle in the system studied, and then numerically integrates equations of motion [36]. Time evolutions of the

system are thus obtained to calculate various properties. Below covers key aspects of MD techniques, and the specific techniques used in this thesis will be described in the method section of chapters 3 and 4.

2.2.1 Protocols for MD Simulations

As presented in figure 2.1 the procedure of MD simulation begins with initial configurations. During this step, initial positions (r), and velocities (v) of all particles in the simulated system should be defined. Then, making use of pre-defined interaction functions $U(r)$, potential energies $V(r)$ and thus forces $F_i = \nabla_i V(r)$ on each atom can be obtained. These forces are used to determine accelerations that are needed to update velocities and positions of the corresponding atom. Along this line, kinetic and dynamic information is outputted for post analysis. This process is repeated until the assigned number of timesteps is reached [37].

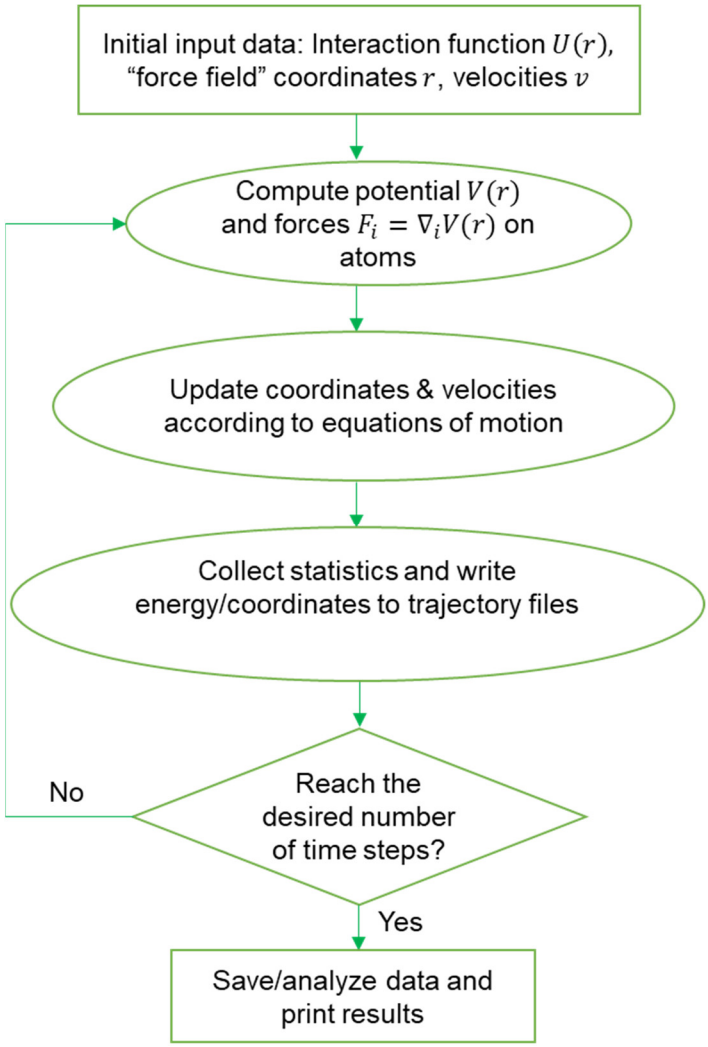

Figure 2.1 Flowchart for MD simulations [37]

2.2.2 Force Fields

As mentioned above, MD calculates forces on each atom based on pre-defined interaction functions. They are a set of equations, and typically referred as force fields or potentials in MD. The total energy contribution in MD simulation is defined as [36]:

$$U_{system} = U_{bond} + U_{angle} + U_{torsion} + U_{coulomb} + U_{vdw} \qquad (2.1)$$

The parameters in equation 2.1 are shown in Figure 2.2 and presented in detail below.

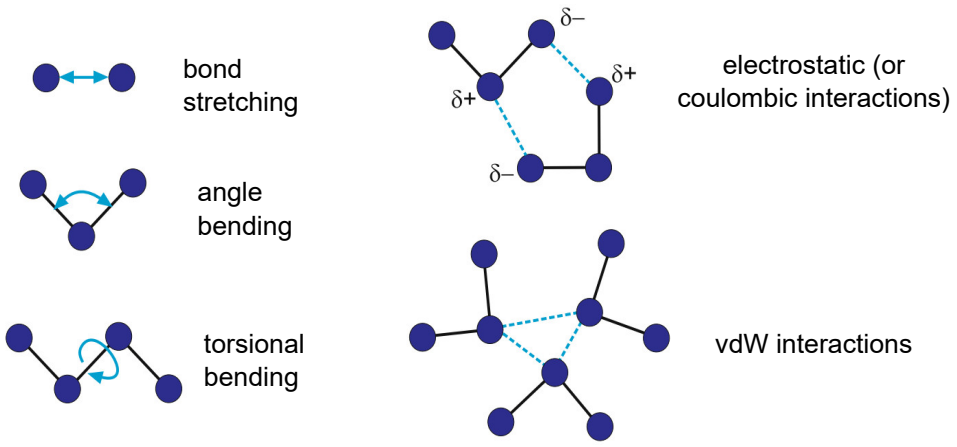

Figure 2.2 Demonstrations of bonds, angles, torsional bending, and non-bonded coulombic and vdW) interactions [38]

The energy related to bond stretching is typically described using [39]:

$$\emptyset(r_{ij}) = a_0 + \tfrac{1}{2}k(r_{ij} - r_0)^2 \qquad (2.2)$$

where a_0 is a constant parameter, k is the spring constant, r_{ij} is the distance between atom i and j, and r_0 is the equilibrium spacing. Similarly, the bond bending between three atoms *i*, *j*, *k* is expressed as:

$$\emptyset_{bend} = b_0 + \frac{1}{2}k_{bend}(\theta_{ijk} - \theta_0)^2 \qquad (2.3)$$

where b_0 is a constant, θ_0 is the equilibrium angle between two position vectors of r_{ij} and r_{jk}, θ_{ijk} is the angle between the three atoms *i*, *j*, and *k*, and K_θ is the angle force constant. Following this, the interaction between four-body bonded atoms (*i*, *j*, *k*, *l*) can be expressed as [39]:

$$\emptyset_{torsion} = t_0 + \frac{1}{2}k_{torsion}(1 - \cos(\theta_1)) \qquad (2.4)$$

where $t_0$is a constant, θ_1 is the torsional angle, and $k_{torsion}$ is the appropriate spring constant which describes the resistance to torsional deformation of a group of atoms. Based on the aforementioned definitions, the total bond, angle, and torsion energy of the system can be described as the summation of the contributions from all pairs of atoms (bond stretching), all triple atoms (bond bending), and quadruples of atoms (bond rotation), respectively:

$$U_{bond} = \sum_{bond} \emptyset_{bond} \qquad (2.5)$$

$$U_{bend} = \sum_{triples} \emptyset_{bend} \qquad (2.6)$$

$$U_{torsion} = \sum_{qualruples} \emptyset_{torsion} \qquad (2.7)$$

For non-bonded interactions, the Lennard-Jones potential introduced in 1924 is widely used to model vdW interactions. For two particles (i and j), it is given by:

$$V_{i,j}^{LJ}(r_{ij}) = 4\epsilon_{ij}\left[\left(\frac{\sigma_{ij}}{r_{ij}}\right)^{12} - \left(\frac{\sigma_{ij}}{r_{ij}}\right)^{6}\right] \qquad (2.8)$$

where σ_{ij} is the diameter or distance at which the vdW potential energy $V_{i,j}^{LJ}$ is zero, r_{ij} is the distance between two interacting particles (i and j), and ϵ_{ij} is the wall depth. For electrostatic interactions, they are defined as:

$$\emptyset_{coulomb} = \frac{q_i q_j}{\epsilon_1 r_{ij}} \qquad (2.9)$$

where q_i and q_j are the partial charges of atoms *i* and *j*, r_{ij} is the distance between two charges, and ϵ_1 is the effective dielectric constant [39]. The total vdW and Coulomb energy is given by:

$$U_{vdW} = \sum_{j\neq i=1}^{N} \sum_{j=i}^{N} V_{i,j}^{LJ}(r_{ij}) \qquad (2.10)$$

$$U_{Coulomb} = \sum_{j\neq i=1}^{N} \sum_{j=i}^{N} \frac{q_i q_j}{\epsilon_1 r_{ij}} \qquad (2.11)$$

Force fields can be categorized into two classes: reactive and non-reactive. In non-reactive force fields, atomic bonds can be twisted or stretched; however, no bond can be broken or newly formed. This is, non-reactive force field can simulate flows, interface behaviors, etc., where phenomena, such as mechanical fractures, are in absent. In contrary, reactive force fields are built to have an additional term that changes the bond strength depending on the test conditions. Therefore, bond-dependent behaviors like mechanical fractures can by studied by using reactive force fields [40, 41].

2.5 MD Algorithms

To integrate equations of motion, various algorithms have been proposed such as Leap-Frog algorithm, Beeman Algorithm, and Velocity Verlet algorithm [42], among which velocity Verlet is widely used in computational packages (e.g., LAMMPS [43] and GROMACS [44]). These algorithms define a stepping method that updates the coordinates and velocities of the atoms from the previous step(s), and in the Verlet algorithm, the stepping route for particle i is [39]:

$$r_i(t_0) \rightarrow r_i(t_0 + \Delta t) \rightarrow r_i(t_0 + 2\Delta t) \rightarrow r_i(t_0 + 3\Delta t) \ldots \qquad (2.12)$$

Here, $r_i(t_0)$ denotes the position of particle *i* at t_0, $r_i(t_0 + \Delta t)$ is the position of particle *i* at $t_0 + \Delta t$, and so forth. By considering the Taylor expansion of the position vectors of particle *i* at $t_0 + \Delta t$ and $t_0 - \Delta t$, the direct link between new positions at $t_0 + \Delta t$ and the old positions and accelerations at t_0 is expressed as the following:

$$r_i(t_0 + \Delta t) = -r_i(t_0 - \Delta t) + 2r_i(t_0) + a_i(t)\Delta t^2 + \cdots \qquad (2.13)$$

In the above, the accelerations can be calculated by considering the Newton's law:

$$a_i = \frac{F_i}{m_i} \qquad (2.14)$$

2.6 Boundary Conditions, Thermostat and Barostat

In MD simulations, systems under studied are of finite sizes, and usually on the order of cubic nanometers. Therefore, to mimic bulk system, periodic boundary conditions (PBCs) are typically employed at least in one or two directions of the simulation boxes. With PBCs, atoms escaping from one side of the box will re-enter the box from the other side of the box, which ensures a constant number of atoms during a simulation run [45].

In addition to mimic bulk systems, MD utilizes thermostat and barostat to control temperatures and pressures, in order to mimic constant temperature and pressure conditions, respectively, employed in experiments. The functioning of these thermostat and barostat is implemented by changing the velocities of particles as well as the box sizes of the system under simulation. The underlying reason is that from

thermodynamics point view, temperatures and pressures are related to particles' velocities and system sizes [40]. Several well-known thermostats are Berendsen, Nose-Hoover, and Anderson temperature coupling, and widely-adopted barostats are Berendsen, Nose-Hoover, and Langevin piston pressure control [36].

Chapter 3. Towards the Design of Robust Multilayer Graphene: Mechanistic Understandings of the Roles Played by Interlayer Interactions[1]

3.1 Introduction

As the thinnest and strongest material ever known, graphene has been used as reinforcements in metal-matrix composites, ceramic-matrix composites, polymer-matrix composites, etc. [46, 47] For instance, Patil et al. [48] showed that reinforcing silica aerogel with monolayer graphene resulted in a four-fold increase in the strength and stiffness of the composites. In the work of Moeini et al. [49], by having 0.3 and 0.5 wt% of graphene fillers, the elastic moduli of epoxy nanocomposites were enhanced to, respectively, almost 2.4 GPa and 2.5 GPa from 2.3 GPa where the matrix was free of graphene fillers. It is noted that these improvements in the Young's modulus were achieved by adding less than 1 wt% of the graphene reinforcement. Given these wide usages, mechanical properties of graphene have attracted tremendous attentions in the literature [50–52].

Single-layer graphene was reported to have a Young's modulus ~1 TPa [1, 7, 53]. Furthermore, the ultimate stress in the zigzag and armchair directions of graphene is ~120 GPa and 100 GPa, respectively, and the ultimate strain in the zigzag and armchair directions is ~0.16 and 0.14, respectively [6,8–11]. For multilayer graphene, it has been reported that increasing the number of graphene layers can reduce the corresponding ultimate strength during tensile tests [11,15]. Zhang et al. [57] performed uniaxial tensile tests, using molecular dynamics (MD) simulations, on monolayer and 7-

[1] This is a preprint of an accepted paper in the Journal of Materials Science, reproduced with permission from Springer Nature.

layer graphene samples. It was revealed that the ultimate stress of graphene showed a minor drop, being from ~117 GPa to ~114 GPa as the number of layers increased to 7 from 1. Using finite element methods, Kordkheili et al. [58] found that the ultimate stress of bilayer graphene was descended by ~3 GPa compared to that of monolayer graphene. On the other hand, the Young's modulus obtained from these uniaxial tensile tests were found to be independent of the number of graphene layers [6,12].

Contrary to that in tensile stretch, Young's modulus exhibits a decrement with increasing the number of layers in nanoindentation tests [7, 59, 60]. Zhong et al. [7] reported that the Young's moduli of the 12-layer and 19-layer graphene sheets were ~960 and ~780 GPa, respectively. This decrement was attributed to the transformation from nano states to bulk states in multilayer graphene. However, no further information was available to address why such transformations can induce decrement, especially given that both 12-layer and 19-layer graphene still resides in nano states. Similar conclusions were obtained in the studies of Neek-Amal et al. [60] on bilayer graphene and Zhang et al. [59] on graphene sheets of thicknesses 10-500 nm. But again, the underlying reasons for these decrements were not provided. Recently, Falin et al. [13] performed nanoindentation tests on multi-layer graphene sheets using atomic force microscopy and finite element methods. Their results revealed that the Young's modulus of graphene sheet is thickness-dependent and shows an overall decrement with increasing the number of layers. Despite that relative sliding was proposed to be responsible for such decrements, there was lack of direct evidence to support the aforementioned claim.

To improve the performance of multilayer graphene, Muniz et al. performed MD simulations on bilayer graphene with interlayer-sp^3 bounded domains. It was reported that while the presence of sp^3 bonds introduced partial deteriorations in the tensile strength and Young's modulus, the shear moduli and load transfer, as well as buckling resistance, were improved [61]. Similar results were obtained by Zhang et al. [62] Specifically, interlayer sp^3 bonds in bilayer graphene were found to improve the shear modulus, load transfer rate, and stability [62]. On the other hand, the presence of sp^3 bonds decreased the Young's modulus and ultimate strength of the bilayer graphene sheets [62]. Furthermore, in the work of Machado et al. [63], MD simulations were performed to investigate the mechanical properties of diamond superlattices generated by interlayer bonding in twisted bilayer graphene. They reported [63] that under tension loading, Young's moduli, shear moduli, and ultimate strengths of these diamond superlattices exhibit a monotonic degradation due to the presence of interlayer bonds. Contrarily, under shear loading, shear moduli were enhanced by interlayer bonds [63].

Our literature review showed that few studies have been focusing on revealing atomistic deformations of multilayer graphene under the influences of non-bonded interlayer interactions. This further leads to the lack of fundamental understandings for the different observations during uniaxial tensile stretch and nanoindentation. To bridge this gap, we performed MD simulations to investigate the mechanical responses of multilayer graphene, where both the number of layers and the strength of interlayer interactions was varied. Compared to similar literature works [7, 13, 64], our focus here is to not only probe and validate potential effects induced by the changes in the number of layers (non-bonded interactions), but also, more importantly, reveal underlying

reasons responsible for these effects through extensive strain analysis. To confirm our findings, we also performed additional simulations on hybrids of graphene and boron nitride (GBN), since it has been proposed in literature that nanosheets composed of BN atoms possess stronger interlayer interactions than multilayer graphene [13, 24]. Furthermore, GBN sheets have promising applications in electronics and structural materials [65, 66]. A summary of the literature review on the mechanical properties of multi-layer graphene is summarized below.

Multi-layer graphene shows thickness dependent mechanical properties. Li et al. [67] measured the in-plane mechanical response of graphene and multilayer graphene by using SEM for the first time. They claimed that the fracture strengths of graphene nanosheets decrease as the thickness or number of layers increases ascribed to the weak vdW forces between adjacent layers, while the fracture strain of thicker graphene sheets is greater than that of thinner sheets. According to the SEM report of Zhang [68], the fracture of pre-cracked bilayer and multilayer graphene happens in a brittle manner, and the fracture toughness quantity is lower than intrinsic strength of graphene. In addition, they proved that at longer cack size, the multi-layer graphene system has lower stress intensity factor (toughness). They measured the toughness of graphene as $4.0 \pm 0.6\ \mathrm{MPa}\sqrt{\mathrm{m}}$. Wei [69] used TEM and measured the fracture toughness of multi-layer (10-layer thick average) graphene as $12.0 \pm 3.9\ \mathrm{MPa}\sqrt{\mathrm{m}}$ that is higher than that of monolayer graphene due to the crack branching and meandering when the thickness increases in the graphene sample. Based on the in-situ uniaxial tension under SEM, Jang et al. [70] calculated the value of Young's modulus for pre-cracked bilayer graphene as 897 GPa. Also, they concluded that the local branching and meandering of

crack paths reduce the driving force of the existing cracks, leading to higher fracture toughness.

Han et al. [71] performed nanoindentation test by using a series of MD simulations and concluded that due to the absence of interlayer sliding in suspended multilayer graphene in the nanoindentation test when the graphene boundaries are clamped, the calculated Young's modulus is insensitive to the number of layers. In contrast, their results of Young's modulus show decrement by sample thickness when the membrane boundaries are weakly clamped and therefore the layers are sliding. Zhong et al. [7] performed the tensile test by suing MD simulation and showed that monolayer and multilayer graphene have the same values of about 1.05 TPa as the Young's modulus. Nevertheless, their MD results of Young's modulus of the suspended multilayer graphene under the nanoindentation test showed a decrement by the number of layers up to a critical thickness. After the critical number of layers of 12 the value of Young's modulus achieved from the nanoindentation showed a sudden drop. They explained this behavior because of the nano-to-bulk transformation of graphene at 12-layer thickness. Chen et al. [72] studied the relation between bending stiffness and interlayer shear interactions of few-layer graphene by ATM. They calculated the value of shear modulus (denoting materials' responses to shear stress) of this few-layer graphene to be in the range of 0.36 to 0.49 GPa. Also, they revealed that there exists a squared-power relationship between the bending stiffness and the graphene samples thickness. Due to weak interlayer shear interactions as a result of vdW forces, few-layer (2-6 layers) graphene showed a stiffening effect.

This chapter is organized as follows: simulation details are introduced in section 3.2-3.4, detailed analysis of simulation results is presented in section 3.4 together with case studies of GBN sheets, and final conclusions are given in section 3.5.

3.2 Simulation Setups

Fig. 3.1 shows the schematic representations of our tensile stretch as well as nanoindentation tests. Our tensile stretch simulations (Fig. 3.1 a) were first performed on graphene sheets with an in-plane $(x - y)$ dimension of 100×100 Å^2 and different thicknesses along the z direction. For indentation simulations (Fig. 8b), graphene was set up as a circular membrane with clamped boundaries and a radius of 50 Å; the indenter was modelled as a rigid sphere with a radius of 10 Å. Furthermore, the contact between the indenter and the graphene was assumed to be frictionless [73–75]. In total, 6 graphene systems were built for tensile tests, each of which has 1-layer, 2-layer, 5-layer, 8-layer, 14-layer graphene, respectively. The same number of layers was adopted in nanoindentations to provide a fair comparison. It needs to be pointed out that these numbers of layers were chosen based on literature works [7, 13] to cover graphene samples with less than 10 layers as well as graphene with more than 10 layers.

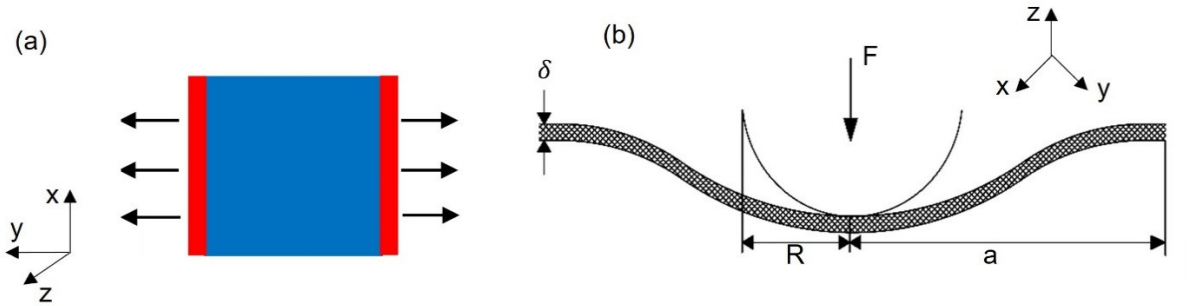

Figure 3.1 Schematic representations of (a) tensile and (b) nanoindentation tests. In (a), the strain is applied in the armchair direction of graphene (along the *y* axis). In (b), *F*

is the applied force along the *z* direction, *R* is the indenter radius, *a* is the membrane radius, and δ is the layer thickness

To validate our findings on interlayer interactions (details in section 3.4), GBN samples were constructed by replacing carbon atoms with boron and nitrogen atoms in the center of each graphene sheet. Boron nitrides are of particular interests here, since it has been proposed in the literature [13, 24] that BN sheets have stronger interlayer interactions than graphene sheets. The radius of BN area was considered to be 2.5 nm, and three samples were built, each containing 1 layer, 2 layers, and 5 layers, respectively (see Fig. 3.2 for representative configurations). Similar configurations of hybrid GBN can be made by using electron beam welding method experimentally [76]. Both tensile and indentation simulations of GBN samples were then performed following the schematics shown in Fig. 3.1.

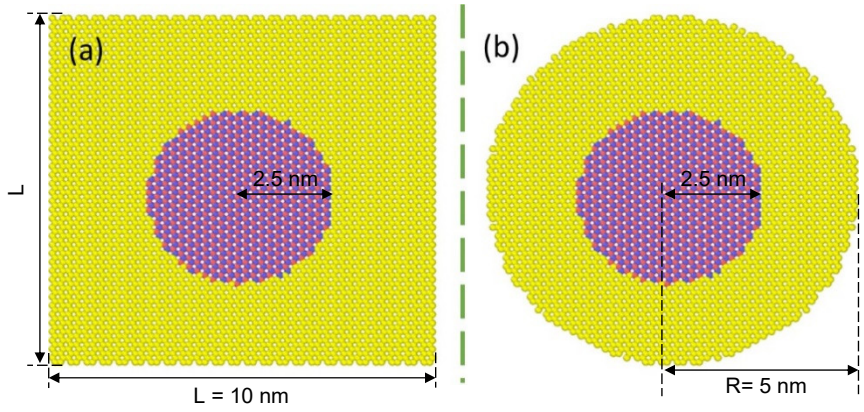

Figure 3.2 Configurations of monolayer GBN in (a) tensile, and (b) nanoindentation simulations. Yellow, red, and purple dots represent the carbon, boron, and nitrogen atoms, respectively

3.3 Simulation Details

Two types of potentials were employed to probe the effect of interlayer interactions on multilayer graphene. The first potential was the Adaptive Intermolecular Reactive Empirical Bond Order (AIREBO) [77], which has been widely used in similar literature works [17, 23–25]. Based on AIREBO, we increased the carbon-carbon nonbonded interaction parameter described in the Lennard-Jones (LJ) potential: $V(r) = 4\epsilon\,[(\sigma/r)^{12} - (\sigma/r)^{6}]$ [81]. Here, V is the intermolecular potential between two atoms, ϵ is the well depth of the potential, σ is the van der Waals radius of carbon atoms, and r is the distance between two atoms. For our purpose, ϵ is increased to 0.02843732471143 eV from 0.002843732471143 eV. We note that these values are defined for atomistic studies, which is different from macroscopic values. In other words, we increased the nonbonded LJ interactions by 10 folds to obtain enhanced interlayer interactions among different layers. It needs to be mentioned that we are focusing on qualitative comparisons here, and the absolute values of interactions should not be of any concerns.

For GBN samples, we first employed the original Tersoff potential, which has been widely used for studying the mechanical properties of hybrid GBN, but lacks parameters for calculating interlayer interactions [42]. This is, GBN sheets were simply stacked together without interacting with one another. Secondly, to include interlayer interaction, nonbonded parameters among carbon, boron, and nitrogen atoms in different layers were adopted from the work of Lee et al. [82], and added to interactions defined in the Tersoff potential.

3.4 Simulation Procedures

Prior to applying load, all systems were first relaxed in the *NVE* ensemble for 100000 steps, followed by relaxation in the *NPT* ensemble for 300000 steps. In *NVE*, the number of particles (N), volume (V), and the energy (E) of the system were kept without change during the equilibration; *NPT* fixed the number of particles (N), pressure (P), and temperature (T) for the simulated systems. After equilibration, uniaxial tensile stretch was performed in the *NPT* ensemble with loading applied in the armchair direction (y direction) and a strain rate of 0.0004 $/ps$ ($4 \times 10^8/s$). Indentation simulations were also performed in the *NPT* ensemble, and an indentation speed of 0.002 $\text{Å}/ps$ (0.2 m/s) was employed. We note that our loading speeds are considerably higher than experimental values [38]. However, it is a standard practice in MD simulations to achieve the desired deformation or indentation depth within a reasonable simulation time [38, 83]. It also needs to be pointed out that our results here are independent of strain rates (comparisons presented in section 3.5.1).

For all simulations, periodic boundary conditions were applied along x and y directions; a timestep of 0.001 *ps* was adopted; temperature was controlled at 300 K using a Nose-Hoover thermostat [84]; and pressure was controlled at 0 bar using a Nose-Hoover barostat [85]. All simulations were performed using LAMMPS (version 29Mar2019) [43], and OVITO (version 3.5.2) [86] was used for visualization as well as certain post analyses.

3.5 Results and Discussion

3.5.1 Time-Dependent Responses of Graphene

Fig. 3.3a plots the stress-strain curves for multilayer graphene under tensile stretch. Simulations performed using the original AIREBO (OA) potential were denoted by 1-OA, 2-OA, 3-OA, 5-OA, 8-OA, and 14-OA, where the number represents how many layers of graphene were present in the simulated systems. On the other hand, simulations performed using LJ increased potential were denoted by LJ postfix. It can be seen that different curves almost overlap with one another, especially the linear parts, irrespective of the number of layers as well as the potentials employed. To examine whether such a phenomenon also holds for multilayer graphene under indentation tests, Fig. 3.3b plots force-displacement curves obtained from simulations performed using both OA potential and LJ increased potential.

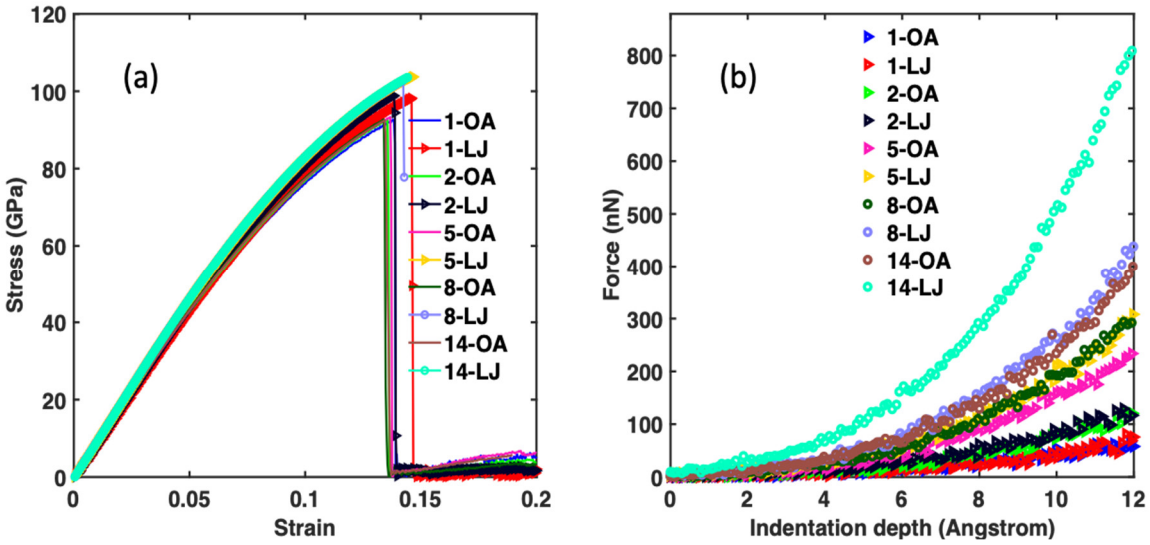

Figure 3.3 a) Stress-Strain plots obtained from the tensile test of multi-layer graphene, and b) Force-displacement plots from the nanoindentation test of multilayer graphene

From Fig. 3.3b, it is clear that both the number of layers and the type of potentials can affect the mechanical responses, evidenced by the non-overlapping

curves. First, with the same type of potential, a smaller indentation force is needed to achieve the same indentation depth for thinner graphene, compared with that of thicker graphene. For example, in 8-OA, an indentation force of ~300 nN is required for the indenter to achieve a depth of 12 $\dot{A}$; in comparison, the indentation force needed by 14-OA is clearly increased to ~400 nN. This observation is consistent with the results reported by Zhong et al. [7] in which it was shown with increasing the number of layers, indentation forces exhibited an monotonic increment at the same deflections. Furthermore, with increased interlayer interactions, while for 1-layer and 2-layer samples, force-displacement curves (denoted by 1-LJ and 2-LJ) overlaps with those obtained using OA potential (denoted using 1-OA and 2-OA), there is a distinct difference existing in the responses of 5-layer, 8-layer, and 14-layer samples. This is, to achieve the same indentation depth, forces needed in 5- LJ, 8-LJ, and 14-LJ, are larger than their counterparts in 5-OA, 8-OA, and 14-OA. It needs to be pointed out that our results here are independent of the indentation speed. To verify this, we increased our indentation speed to 0.04 $\text{Å}/ps$ and the corresponding force-displacement curves are shown in Fig. 3.4. As can be seen, for the same sample, these curves essentially overlap with each other, suggesting that indentation speeds do not significantly affect mechanical responses of graphene. It is also worth noting that 1-OA and 1-LJ at the two speeds all overlap with one another. Thus, we emphasize that this observation holds for samples with the original AIREBO (OA) as well as those with increased interlayer interactions (LJ).

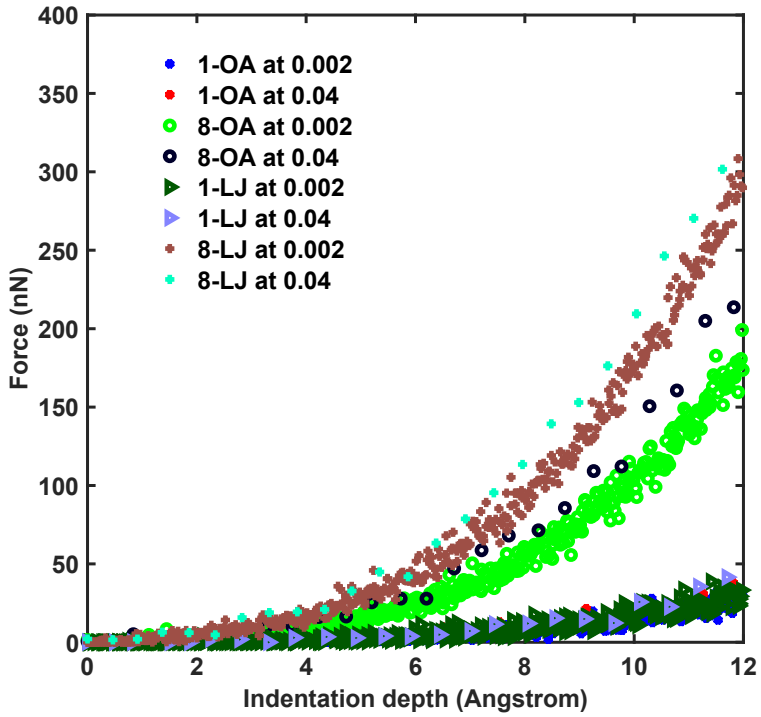

Figure 3.4 Force-displacement graphs obtained from the nanoindentation simulation of monolayer and 8-layer graphene at different indenter speeds

3.5.2 Young's Moduli of Graphene

The above observations seem to suggest that interlayer interactions played different roles in the tensile stretch and indentation tests. To confirm this, we further calculated Young's modulus in each case. For the uniaxial tensile stretch, the following equation was used to fit the stress-strain curve [7]:

$$\sigma = E\varepsilon + D\varepsilon^2, \qquad (3.1)$$

where σ represents stress, ε represents strain, E denotes the Young's modulus (the slope of the linear portion in the stress-strain curve), and D denotes third-order elastic modulus, respectively. For indentation tests, the force-displacement behaviors were described using [7, 87]:

$$F = c\delta + d\delta^3. \qquad (3.2)$$

in the above equation, *F* is the indentation force, δ is the displacement of the indenter, and coefficients *c* and *d* are defined as follows:

$$c = \sigma_0 \pi h (R/a)^{3/4}, \quad (3.3)$$

$$d = Eqa^{-2} h (R/a)^{1/4}, \quad (3.4)$$

where σ_0 is the pretension, *R* is the indenter radius, *h* is the thickness of multilayer graphene, *a* is the radius of graphene samples, *E* is Young's modulus, and *q* is a dimensionless factor and equal to $9\pi/16$ according to the model developed in the work of Begley and Mackin [88, 89].

Table 3.1 summarizes Young's moduli obtained. For a single-layer graphene, the Young's modulus in LJ systems is slightly increased compared to the counterpart in OA systems, due to the increased non-bonded interactions in LJ systems. It needs to be noted that non-bonded interactions universally exist among any two atoms and are present in all graphene samples, while interlayer interactions, originating from non-bonded interactions, refer to non-bonded interactions among different layers and thus exist in graphene samples with at least two layers. More importantly, as expected, during the tensile stretch, the Young's modulus of graphene is independent of the number of layers as well as the potential employed. This is consistent with the results reported in the work of Zhong et al.[7], where it was found that the Young's modulus from the tensile stretch is not sensitive to the number of layers. Contrarily, for samples under indentation tests, with increasing the number of layers, the Young's modulus shows an overall decrement. For instance, the Young's moduli for 2-OA and 8-OA graphene samples are, respectively, 0.85 TPa and 0.59 TPa. Similar observations are also reported in the work of Falin et al. [13] Furthermore, for a given number of layers,

with increasing interlayer interactions, the Young's modulus is increased. This is particularly evident for 8-layer and 14-layer samples, where the Young's modulus was increased by 36 % from 8-OA to 8-LJ, and 100% from 14-OA to 14-LJ. This enhancing effect of interlayer interactions shares similarities with the work of Falin et al. [13] In their work [13], it was proposed that unlike graphene, Young's moduli of BN sheets show less dependence on the number of layers, which is originated from the stronger interlayer interactions exist among BN sheets than those among graphene layers. For our results here, to understand these different roles of interlayer interactions, below we will take a look at strain distributions in different samples.

Table 3.1 Young's moduli calculated for samples under uniaxial tensile stretch and nanoindentation tests

Samples	1-OA	1-LJ	2-OA	2-LJ	5-OA	5-LJ	8-OA	8-LJ	14-OA	14-LJ
Tensile (Unit: TPa)	0.84	0.85	0.85	0.89	0.87	0.92	0.88	0.93	0.87	0.93
Indentation (Unit: TPa)	0.90	0.93	0.85	0.9	0.71	0.86	0.59	0.8	0.42	0.84

3.5.3 Strain Distributions

During the tensile stretch, since the strain was applied in the armchair direction, i.e., the y direction, yy strain (ε_{yy}) distributions were analyzed for each layer in multilayer graphene. This is, ε_{yy} represents the normal strain. Representative results were plotted in Fig. 3.5 using distributions in 8-OA and 8-LJ. First, the localized small/large strains appear in a random manner, and overall, a uniform distribution is presented for ε_{yy}. Secondly, the comparison between a) and c), as well as between b)

and d), shows no considerable differences. These observations suggest that interlayer interactions play insignificant roles in affecting the distribution of normal strains. As a result, both stress-strain behaviors and Young's moduli are insignificantly affected. Similar observations were obtained for other samples.

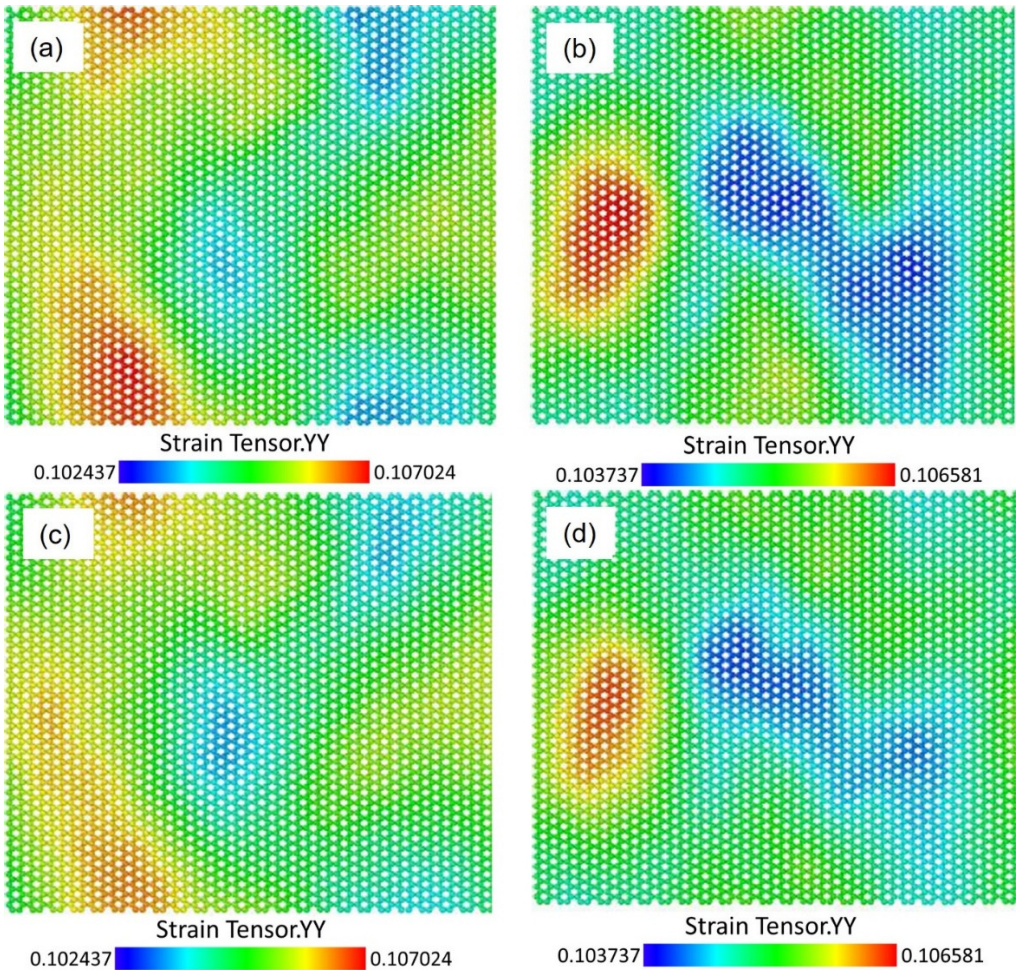

Figure 3.5 Distributions of ε_{yy} at simulation time *t* = 250 *ps* in a) the topmost layer of 8-OA, b) the topmost layer of 8-LJ, c) the third layer of 8-OA, and d) the third layer of 8-LJ

For samples under indentation tests, our analysis was performed on shear strain distributions, since it has been proposed that relative sliding can occur between different layers [13]. Here, the shear strain is defined as [89]:

$$\tau = [{\varepsilon_{xy}}^2 + {\varepsilon_{xz}}^2 + {\varepsilon_{yz}}^2 + 1/6\left(\varepsilon_{xx} - \varepsilon_{yy}\right)^2 + (\varepsilon_{xx} - \varepsilon_{zz})^2 + \left(\varepsilon_{yy} - \varepsilon_{zz}\right)^2]^{1/2}. \quad (3.5)$$

here, τ denotes the shear strain; ε_{xx}, ε_{yy}, and ε_{zz} are the tensor components along the x, y, and z directions, respectively; and ε_{xy}, ε_{xz}, and ε_{yz} are the Green-Lagrangian strain tensor components in the xy, xz, and yz planes, respectively. Representative results of shear strain distributions were shown in Fig. 3.7 based on 8-OA and 8-LJ.

Clearly, different patterns can be observed. For the first layer in 8-OA (Fig. 3.6a), shear strain is highly localized at the geometry center of the corresponding layer, which is directly underneath the indenter tip. In the case of 8-LJ (Fig. 3.6b), this localization of shear strain is weakened and shifted towards the boundary of the sample. Moving to the second layer, although the maximum strain is decreased in 8-OA (Fig. 3.6c), the localized strain is still present near the geometry center of the sample. On the other hand, 8-LJ (Fig. 3.6d) has a ring-like localization of shear strain, and the value of shear strain is much reduced near the geometry center. As for the fourth layer (Fig. 3.6e and 3.6f), both 8-OA and 8-LJ have reduced shear strains near the geometry center. Actually, for 8-LJ, the shear strain reduced to almost zero near the geometry center, indicating reduced relative sliding with respect to other layers and suggesting increased resistance to loading due to the increased interlayer interactions. This observation, where the shear strain was shifted away from the geometry center, is similar to the strain shielding observed in the work of Kumar et al. [64] In that work [64], it was proposed that the interaction between the indenter and graphene can move shear strain along the radial direction of graphene samples. In our work here, the interlayer interactions, particularly in 8-LJ case, should be responsible for the strain shifting observed, which ultimately reduces the strain concentration near the geometry center of

multilayer graphene underneath the indenter tip. Shear strain distributions obtained at different speeds are shown in Fig. 3.7 using 1-layer and 8-layer samples as representative examples. As can be seen, while the shear strain values are slightly different, the distributions obtained at the two speeds have very similar patterns, again demonstrating that indentation speeds do not significantly affect mechanical responses.

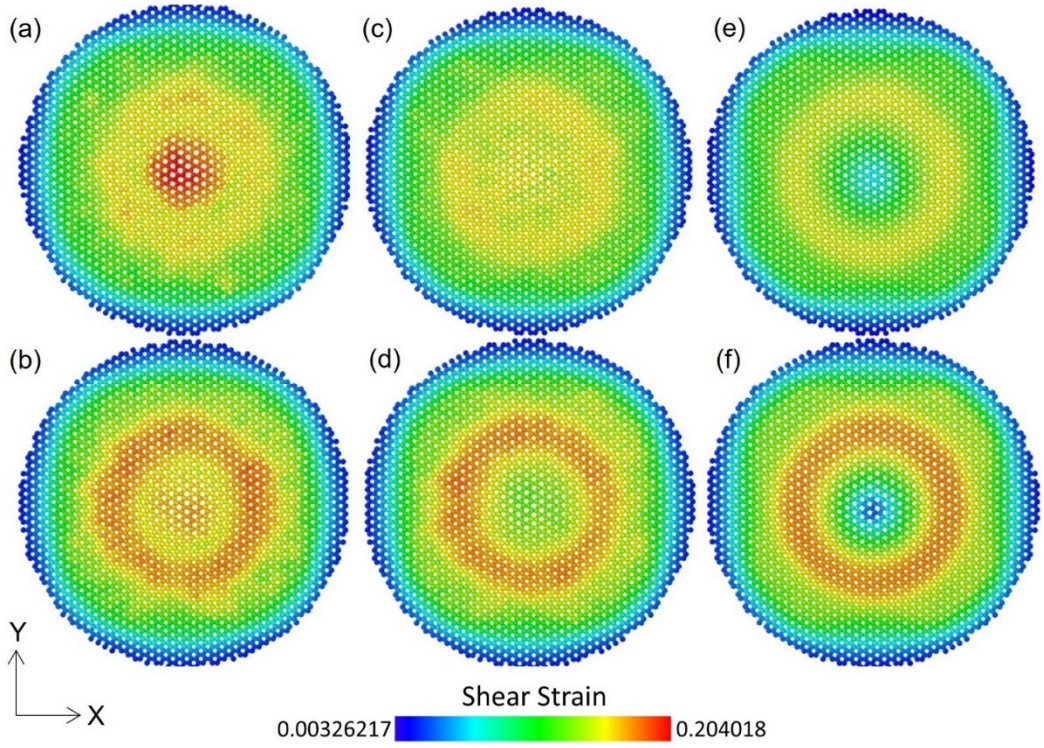

Figure 3.6 Shear strain distribution at simulation time $t = 7000$ *ps* in a) the first layer of 8-OA, b) the first layer of 8-LJ, c) the second layer of 8-OA, d) the second layer of 8-LJ, e) the fourth layer of 8-OA, and f) the fourth layer of 8-LJ

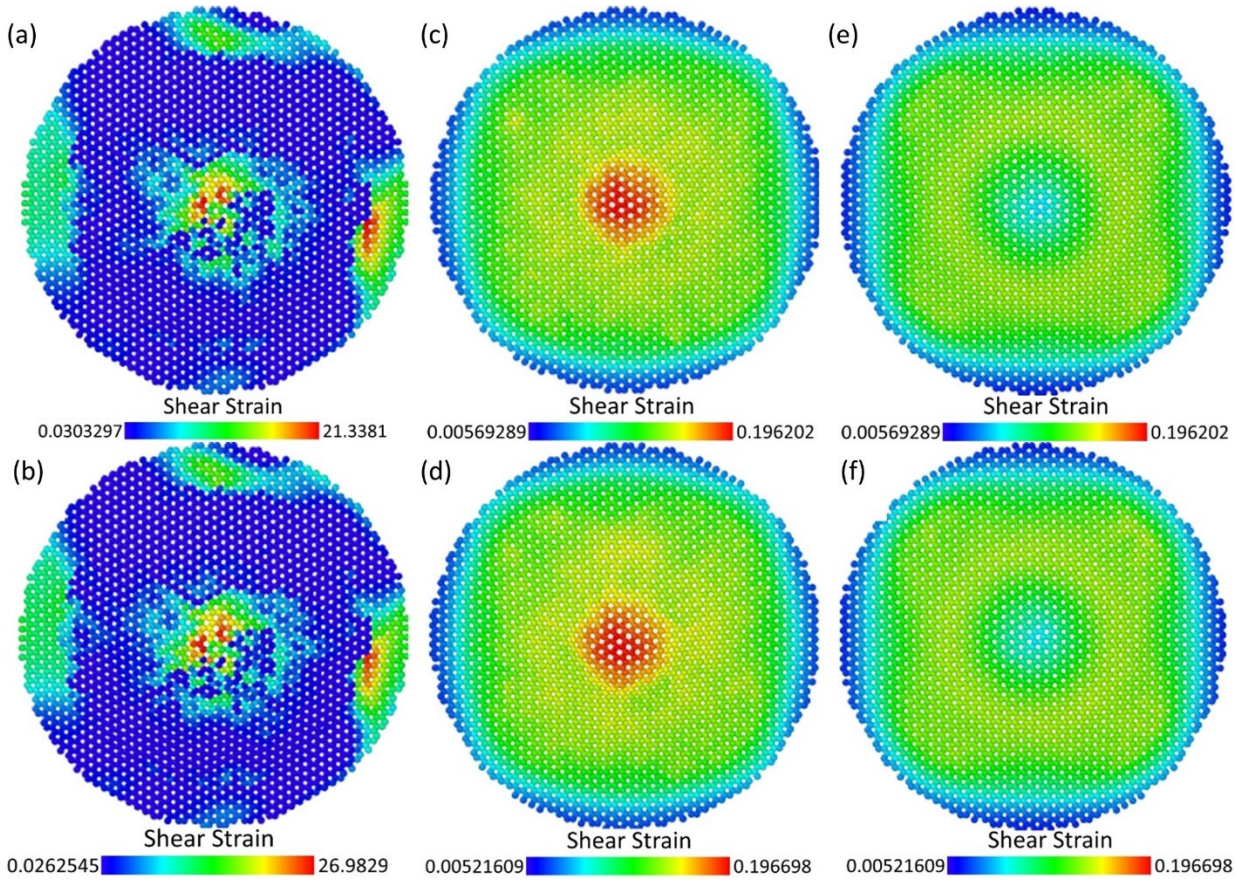

Figure 3.7 Shear strain distribution over graphene layers achieved at two indenter speeds: a) 1-OA at 0.002 Å /ps, b) 1-OA at 0.04 $Å/ps$, c) 8-OA first layer at 0.002 $Å/ps$, d) 8-OA first layer. at 0.04 $Å/ps$, e) 8-OA fourth layer at 0.002 $Å/ps$, and f) 8-OA fourth layer at 0.04 $Å/ps$. The visualizations obtained at an indentation depth of 16.65 Å and 18.5 Å for monolayer and 8-layer graphene samples, respectively

To quantitively show differences between the shear strain distributions, we further analyzed the radial distributions of the shear strain and plotted them in Fig. 3.8 based on results from 8-layer sample. As can be seen, shear strains in 8-OA samples show an overall decreasing trend from the central region of graphene to its clamped edges. On the other hand, 8-LJ samples exhibit more complex patterns. For the first layer in 8-LJ, at r = 0 where the indenter contacts the first layer of graphene, the shear strain is highest. Moving away from the central region, the shear strain is reduced in 8-

LJ due to the reduced sliding with an enhanced interlayer interaction. Further approaching graphene boundaries, the shear strain is increased again because of the fixed boundary conditions (clamped edges), i.e., no shear strain at r = 50 Å. For the fourth layer in 8-LJ, both central regions and clamped edges have very low shear strains, which are resultant from the enhanced interlayer interactions and the specific boundary conditions, respectively. Meanwhile, the highest shear strain appears in the middle region inclining to the clamped edges, due to the fixed boundary conditions. The effect of interlayer interaction in reducing in shear strain is also evident when comparing 8-OA and 8-LJ as discussed below.

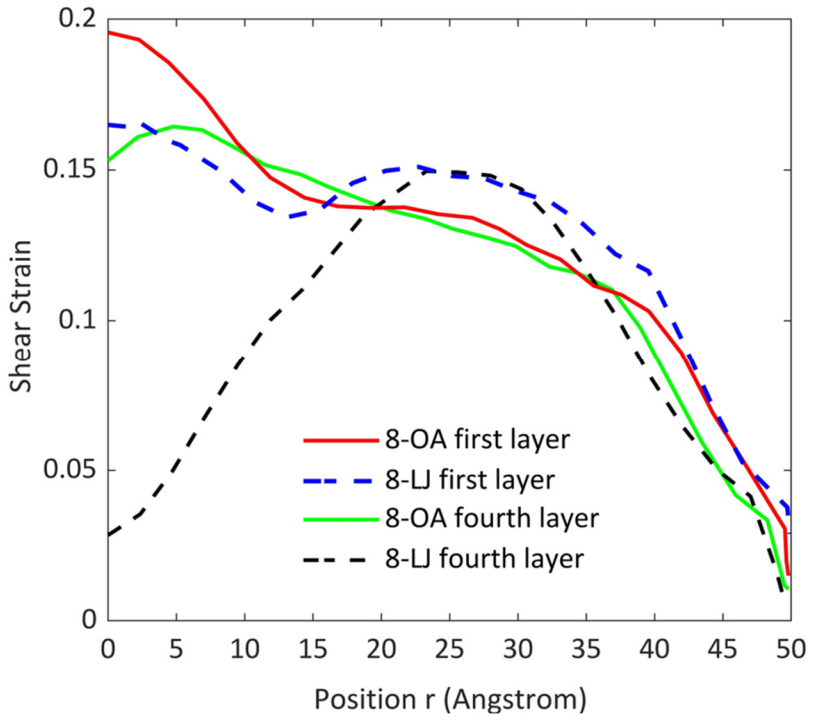

Figure 3.8 Shear strain distribution along radial direction for the first layer and the fourth layer at $t = 7000$ ps

For the first layer, compared to that in 8-OA, the value of shear stain near the geometry center (*r=0*) was much reduced in 8-LJ. Furthermore, this reduction near *r=0* is more evident when comparing the fourth layers due to the increased resistance to

indentation in 8-LJ. This is, increasing LJ interactions can help to decrease the concentration of shear strain near the geometry center and thus reduce relative interlayer sliding. As a result, the Young's modulus of 8-LJ is apparently larger than that of 8-OA (table 3.1). Similar observations were obtained for other samples. Overall, increasing interlayer interactions decreased the dependence of Young's moduli on the number of layers (table 3.1). We note that with a different value of ϵ (details in section 3.2), the absolute values of forces and strains will be changed. However, the qualitative comparisons, as well as the conclusions, presented here still stand and should be of no concerns, as long as the ϵ values adopted are of the same orders of magnitudes with our choice here. We also point out that our observations and conclusions do not depend on the numbers of graphene layers. This is, as long as the multilayer graphene still resides in the nano region, a decrement trend will be observed on the Young's modulus with increasing the number of layers [7, 13], and interlayer interactions are responsible for this decrement. To further validate our findings, below we will present simulation results of GBN samples.

3.6 Demonstrations Using GBN Samples

Fig. 3.9 shows the stress-strain relationships from tensile simulation performed on GBN, where results of the original Tersoff potential were denoted using 1-OT, 2-OT, and 5-OT, and results obtained by taking interlayer interactions into considerations were denoted using 2-IT, and 5-IT. As can be seen, the initial portion (up to strain ~0.04) of the stress-strain curve for each system overlaps with one another regardless of the potentials used. Beyond this range and up to the fracture strain, these curves are also close to each other. Furthermore, the maximum stress of each sample is close,

confirming the insignificant effect of interlayer interactions on the tensile responses of GBN samples. We note that once fracture occurs, stress-strain curves of 2-IT and 5-IT show stepwise behaviors, suggesting an asynchronous breaking behavior that might result from the anisotropy of the hybrid GBN samples. Similar phenomena were also observed in the work of Liu et al. [90], as well as the study of Muniz et al. [61], performed on twisted bilayer graphene, where anisotropy was introduced by twisting stacking orientations of graphene sheets.

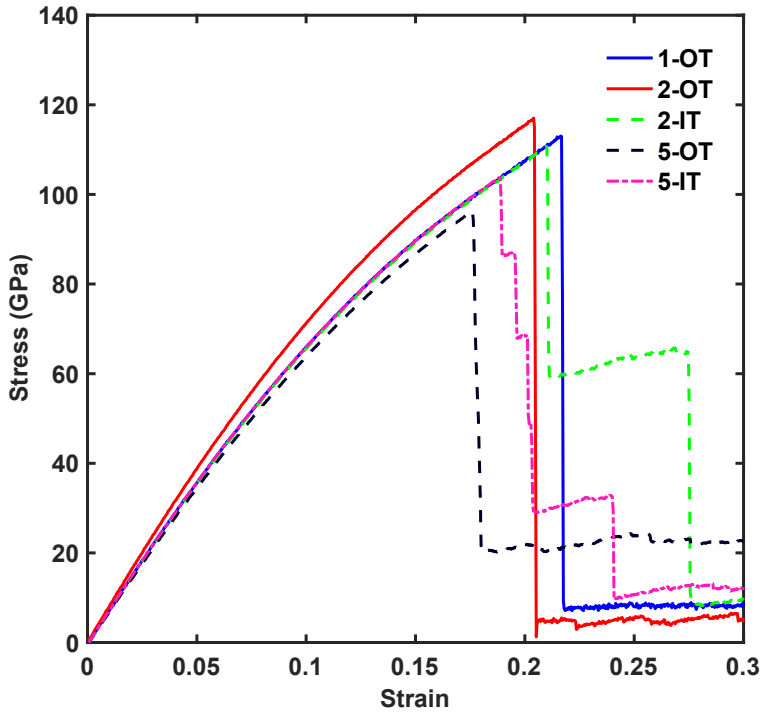

Figure 3.9 Stress-Strain plots obtained from the tensile test of multi-layer GBN

Results from nanoindentations performed on GBN are shown in Fig 3.10. First, with the original Tersoff potential where the interlayer interactions are not included, the force-displacement curves of 1-OT, 2-OT, and 5-OT are almost overlapping with one another. After taking interlayer interactions into account, the thickness-dependent

behaviors of force-displacement curves are clearer. For instance, at an indentation depth of 10 Å, the indentation force needed in 5-IT is ~200 nN, apparently higher than its counterpart (~50 nN) in 5-OT. Furthermore, with incorporating BN, the 5-layer GBN sheets have a Young's modulus ~0.80 TPa, which is higher than that (0.71 TPa) of 5-layer graphene (5-OA in Table 3.1). It is important to note that while pure BN sheets have a smaller Young's modulus than pristine graphene, doping graphene with BNs can help to reduce the decrement of Young's modulus during nanoindentation because of the large interlayer interactions provided by BNs. To further probe this, shear strain distributions in 5-OT and 5-IT are shown in Fig. 3.11.

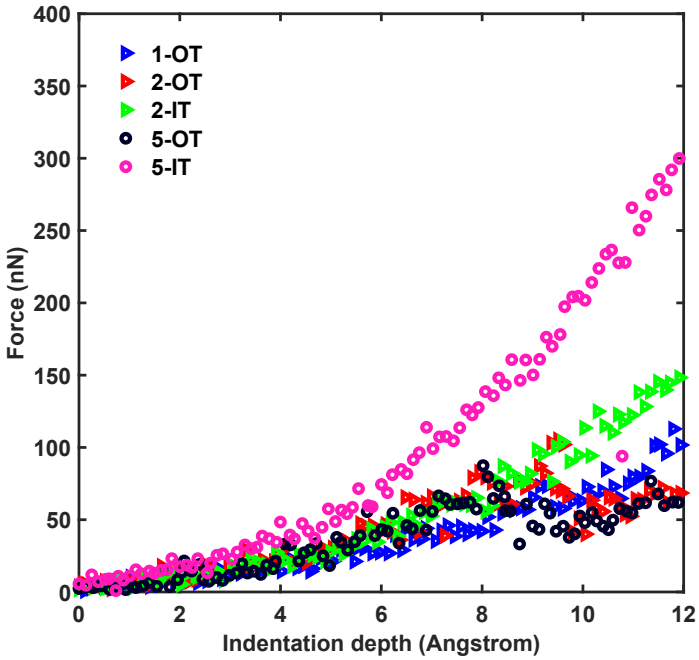

Figure 3.10 Force-displacement plots from the nanoindentation test of multilayer GBN

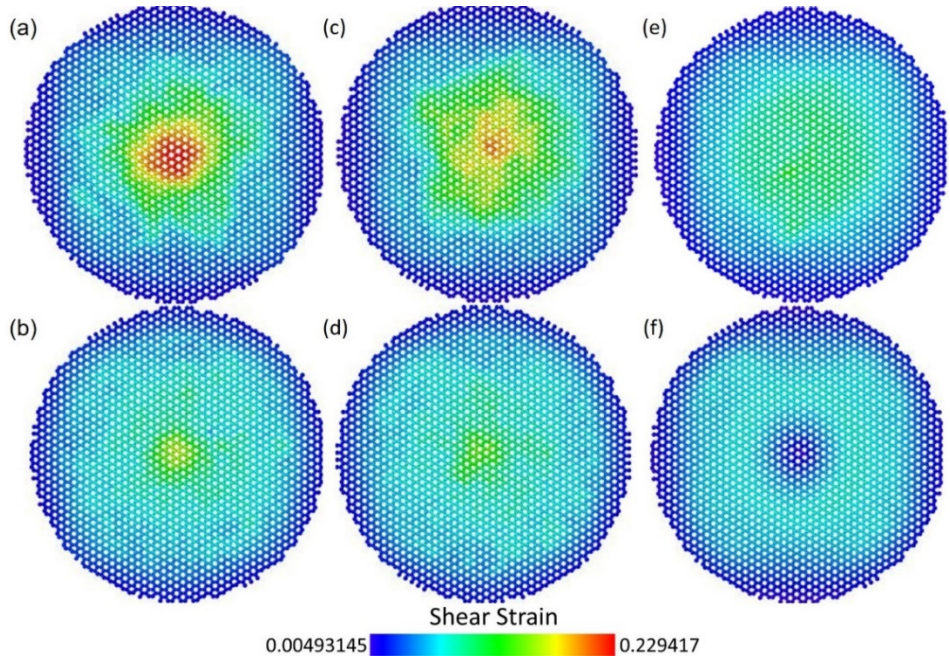

Figure 3.11 Shear strain distributions achieved from the nanoindentation of GBN at simulation time $t = 5000$ *ps* in a) the topmost layer of 5-OT, b) the topmost layer of 5-IT, c) the second layer of 5-OT, d) the second layer of 5-IT, e) the third layer of 5-OT, and d) the third layer of 5-IT

From Fig. 3.11, it can be seen that at in the absence of interlayer interactions (5-OT), the shear strain is mostly concentrated in the area where the indenter contacts the GBN sheet. With the presence of interlayer interactions, strain concentrations are significantly decreased. Especially in the third layer, the maximum strain is actually shifted towards the boundary of the GBN sheets, confirming reduced relative sliding with respect to other layers. This is, strain shielding phenomena, originated from strong interlayer interactions, are clearly present in GBN samples, suggesting increased resistance to loading because of the increased interlayer interactions. We note that these interactions enhanced by doping improve shear performances (Figs. 17 and 18) with little detriment on tensile properties (Fig. 16), which provides guidelines for designing mechanically robust multilayer graphene.

3.7 Conclusion

In this chapter, a series of MD simulations was performed to investigate the mechanical properties of multilayer graphene under different conditions, and further elucidate fundamental mechanisms for the effects of non-boned interlayer interactions. Two potentials were employed, with one being the original AIREBO potential, and the other of increased Lennard-Jones interactions (i.e., increased interlayer interactions). It was found that with both potentials, the number of layers has negligible effects on the stress-strain behaviors and Young's moduli obtained from uniaxial tensile stretch. Further strain analysis demonstrated that the normal strain along the stretch direction has a nearly uniform distribution, and is independent of the interlayer interactions. Contrarily, during nanoindentation, both the number of layers and the potentials can affect the force-displacement responses and Young's moduli. Increasing the number of layers demanded larger indentation forces at the same indentation depth, and meanwhile decreased the Young's modulus. On the other hand, increasing interlayer interactions leads to an increment in both indentation forces and Young's moduli. Shear strain analysis revealed that strain shifting from geometry centers is more prominent with increased interlayer interactions, resulting in the reduced strain concentration near the geometry center, and finally leading to lager indentation forces and Young's moduli. These findings were then validated using hybrid GBN nanosheets, where graphene was doped by BNs. It was demonstrated that during nanoindentation, compared to pristine graphene sheets, the stronger interlayer interactions provided by BNs in the hybrids can help to reduce the decrement in Young's moduli induced by the number of layers.

Chapter 4. Molecular Dynamics Investigations on Graphene Reinforced Polyethylene Nanocomposites

4.1 Introduction

This chapter aims to study the reinforcing role of graphene in composites under different loading conditions. Polyethylene (PE) is chosen here as the matrix for composites, given its wide applications in food packaging, automotive components, medical products, etc. Furthermore, PE is durable, rigid, recyclable and highly adaptable. Therefore, the mechanical properties of this material are of great interests [12].

In the literature, PE/G composites have been widely studied. Li et al. [52] performed MD simulations to investigate the effects of temperature, strain rate, and polymer length on the tensile deformation of polyethylene/graphene (PE/G) composites. Their results revealed that the yield strength of PE/G nanocomposites at higher temperatures and lower strain rates is lower than that at higher strain rates and lower temperatures. In addition, it was reported that longer PE molecules lead to higher yield strength. Rahman et al. [91] studied the deformation behavior of graphene sheets in PE/G nanocomposites by using MD simulations. According to their results, incorporation of graphene enhances the overall Young's modulus and tensile strength of PE/G nanocomposites. In addition, randomly oriented graphene sheets bring in superior properties to the nanocomposite, compared to other spatial arrangements of graphene. For agglomerated or stacked graphene fillers, their results revealed that the mechanical performance of the nanocomposite is dependent on the direction of the applied strain

[91]. Experimentally, Alasvand et al., [92] studied the mechanical properties of graphene reinforced epoxy under tensile and compression tests. Their results also revealed that distributions of graphene can affect the Young's modulus and compressive modulus of the nanocomposites.

In addition to the above studies focusing on external conditions and bulk materials, large amounts of works have also been performed to probe the interface formed between graphene and PE. Degirmenci et al. [93] studied the tensile behavior of nanoporous polyethylene reinforced with carbon-based materials (graphene flakes, fullerenes, and carbon nanotube) through MD simulations. Enhancements in Young's modulus, yield strength, and ultimate tensile strength were observed for all types of fillers, and graphene was the most promising reinforcement for nanoporous PE matrix, due to the highly effective load transfer resultant from the large surface area of graphene. Liu et al. [94] employed united atom MD simulation to study the toughness behavior of PE/G composites. It was found that enhanced interactions between graphene and PE help to increase the toughness of the nanocomposite. Rissanou et al. [95] studied the structural and dynamical properties of PE/G nanocomposites through MD simulation. They reported that the overall mechanical behavior of PE/G nanocomposites is dependent on the spatial heterogeneities created by PE/G interfaces. Specifically, mass density of PE near the graphene phase was maximum due to PE/G interaction. Also, PE chains near the interface were found to be parallel to the graphene sheet, and away from the interface, PE chains prefer random configurations. Thus, PE molecules close to the graphene sheet have slower chain

dynamics. These studies suggest that interfaces formed between graphene and PE plays important roles in determining the mechanical properties of the composites.

Verma et al. [96] studied the effect of grain boundaries (GB) on the interfacial behavior of PE/G nanocomposite using MD simulation. They performed tensile simulation and reported that wrinkled, bi-crystalline graphene containing mis-orientation angle GB can provide increased adhesion points and intensified non-bonding interactions between polymer and graphene, and thus increasing the tensile strength of the nanocomposites. Liu et al. [97] analyzed the interfacial cohesive strength and interfacial shear strength in PE/G nanocomposites. Their results revealed that the interfacial cohesive strength decreases with increasing the grafting density of PE and its chain length, due to the separation of graphene from PE matrix. In contrast, the interfacial shear strength shows complex dependences. On the one hand, it increases with larger grafting density of short PE chains, due to increase of roughness and interlocking effect; on the other hand, the interfacial shear strength decreases with the chain length, because of the reduction of interlocking effect in long PE chains. Truong et al., [98] studied the fracture mode of graphene nanoplatelets reinforced polymer composites. Their results revealed that changing the interfacial alignments between polymers and graphene could help to delay the initiation of crack propagation.

Despite the above works, dynamical responses of PE/G composites have not been reported in detail, especially for the reinforcing role of graphene played at different stages of the deformations. Therefore, in this chapter, PE/G composites were explored at different indentation speeds as well as different indentation depths.

4.2 Simulation Setups

Figure 4.1 shows the schematic representations of the PE chain structure, as well as the nanocomposites samples in the tensile stretch and nanoindentation tests.

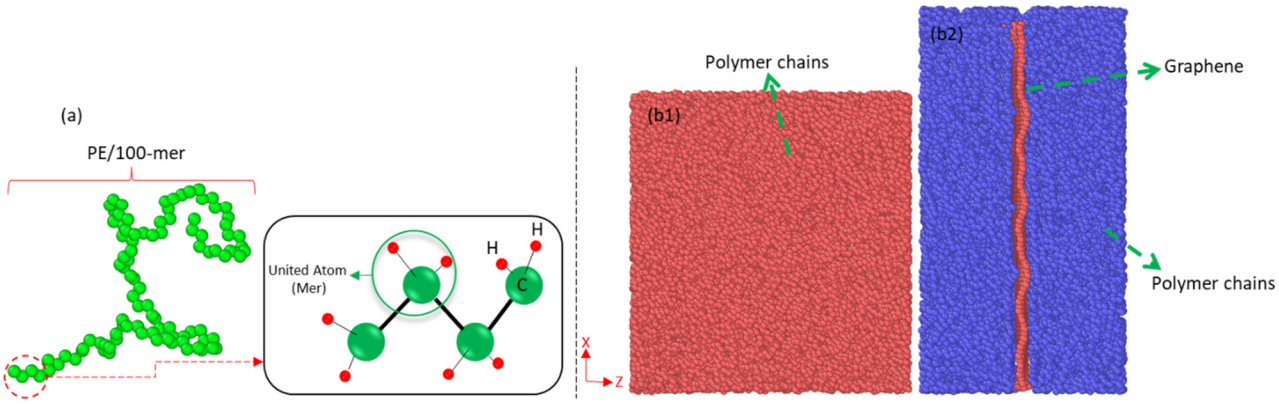

Figure 4.1 Schematic representations of a) PE chain, b1) PE matrix in the tensile test, and b2) PE-nG (n=2,3 layers of graphene) nanocomposites in the nanoindentation simulation

Table 4.1 lists the structural information for all the systems studied in this chapter. Here, 2000 chains with each of 100 units (united CH_2 atoms), and 200 chains of 100 units (united CH_2 atoms) were denoted by 2000/100-mer and 200/100-mer. These systems are constructed to validate models and force fields. Composites of two-layer and three-layer graphene are denoted by PE2G, and PE3G, respectively. These compositions allow to probe the reinforcing roles of graphene under different conditions. We also note that number of PE chains are different in PE2G and PE3G, which will allow us to study the effect of chain numbers as well as different interaction energies (see section 4.4 for details).

Table 4.1 System details

sample	No. of atoms	sample	No. of PE atoms	No. of graphene atoms
200P100-mer	20000	PE2G	8100	7872
2000/100-mer	200000	PE3G	5200	11808

4.3 Simulation Details and Procedures

The carbon and hydrogen atoms in polyethylene monomers were considered as united particles as shown in figure 4.1. The interaction forces between these united particles were modeled using Dreiding force field [19]. Graphene was modeled using AIREBO potential [99]. Interactions between graphene and polymer matrix were taken from the works by Hossain et al., [19] and Chen et al., [100].

Prior to applying load, all systems were undergone four sets of relaxations. The systems were first relaxed in the NVE ensemble for 130,000 ps, followed by relaxation in the NPT ensemble for 315,000 ps. Here, the pressure was controlled at 20 bars, and the temperature was controlled at 500 K in order to fully relax long polymer chains. Afterwards, these samples were cooled down from 500 K to 250 K, followed by a re-equilibration at 250 K in NVT ensemble for 265,000 ps.

After relaxation, tensile simulations were performed on PE systems, and nanoindentation simulations were performed on PE2G and PE3G. For uniaxial tensile stretch, the system was applied with a strain rates of 10^9 S^{-1} in the NPT ensemble. The purpose of these tensile simulations is to validate the PE models. The nanoindentation simulations were also performed in the NPT ensemble with two indentation speeds, 1 and 10 Å/*ps,* to probe the loading effects. The indenter radius was set as 10 Å, and the indenter was considered as a rigid sphere with no interactions with PE2G/PE3G. While

our loading speeds are considerably higher than experimental values, this is a standard practice in MD studies to achieve certain deformations within a reasonable simulation time [7].

For all tensile simulations, periodic boundary conditions (PBCs) and a time step of 0.5 *ps* were adopted. For all nanoindentation simulations, PBCs were applied in x and y direction, and a timestep of 0.001 *ps* was used. The smaller timestep in the nanoindentation is due to the AIREBO potential used for graphene, which is reactive and demands a smaller timestep (also see chapter 3). In all simulations, temperatures and pressure were controlled using Nose-Hoover thermostat and barostat [36]. All simulations were performed with LAMMPS (version 29/Mar/2019) [43]. OVITO software (version 3.6.0) was used for visualization and post analysis [86].

4.4 Results and Discussion

Figure 4.2 plots the stress-strain curves for 2000/100-mer and 200/100-mer PE systems under tensile stretch. It can be seen that the two curves overlap with one another in the linear part, irrespective of the number of PE chains. Also, the more number of PE chains results in a higher ultimate strength value of the system. The results achieved in here are in accordance with the ones reported by Hossain et al., [19] where the same simulations and test conditions were applied. It was reported that chain length and number of chains have little effect on the stress-strain behaviour of PE. Also, they found that the maximum stress is close to 100 MPa for both 200/100-mer and 2000/100-mer systems, which is in excellent agreement with our results plotted in figure 4.2. This finding confirms the accuracy of our method for equilibrating and modelling PE systems. In the following sections, PE/G composites will be

analyzed in detail. Moreover, our estimation of the Young's moduli for 200/100-mer and 2000P/100-mer is about 1.4 GPa. As can be seen, this elastic modulus is much lower than that of graphene (see chapter 3).

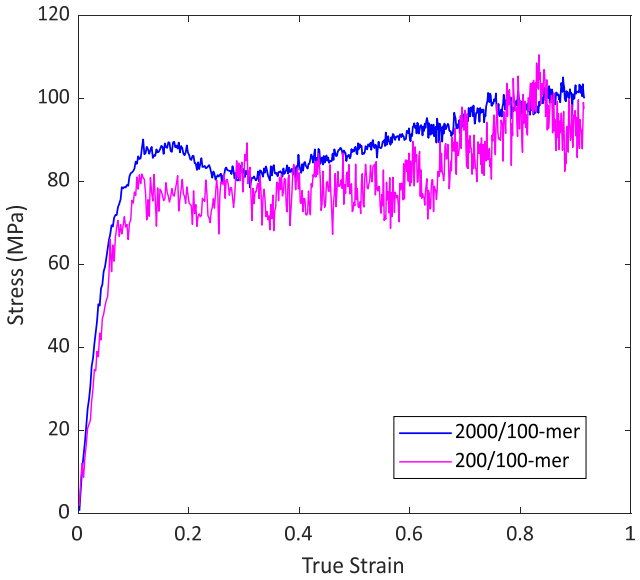

Figure 4.2 Stress-strain responses for different numbers of chains at a strain rate of 10^9 S^{-1} and at 250 K

Figure 4.3 plots the force-indentation depth curves for the graphene reinforced PE composites system under the nanoindentation loadings. Two indenter speeds, 1 and 10 $\text{Å}/_{ps}$, were chosen. With an indenter speed of 1 $\text{Å}/_{ps}$ (figure 4(a)), both PE2G and PE3G show an overall increasing trend. However, subtle differences exist. The responses of PE2G are evident as soon as indentation occurs, due to the existence of a larger number of PE chains. These PE chains also lead to that at a smaller indentation depth, PE2G has a larger force. In contrast, PE3G has evident responses after an indentation depth of 2 Å. This can be attributed to the smaller number of polymer chains in PE3G (see table 4.1). However, after ~ 9 $\dot{A}$, the indentation force in

PE3G surpasses PE2G. Similar behaviors are observed with an indenter speed of 10 $\text{Å}/_{ps}$ as shown in Figure 4.3(b). To analyze the underlying reasons for the behaviours observed above, we calculated the interaction energy between graphene and polymer, as well as stress/strain distributions in these samples.

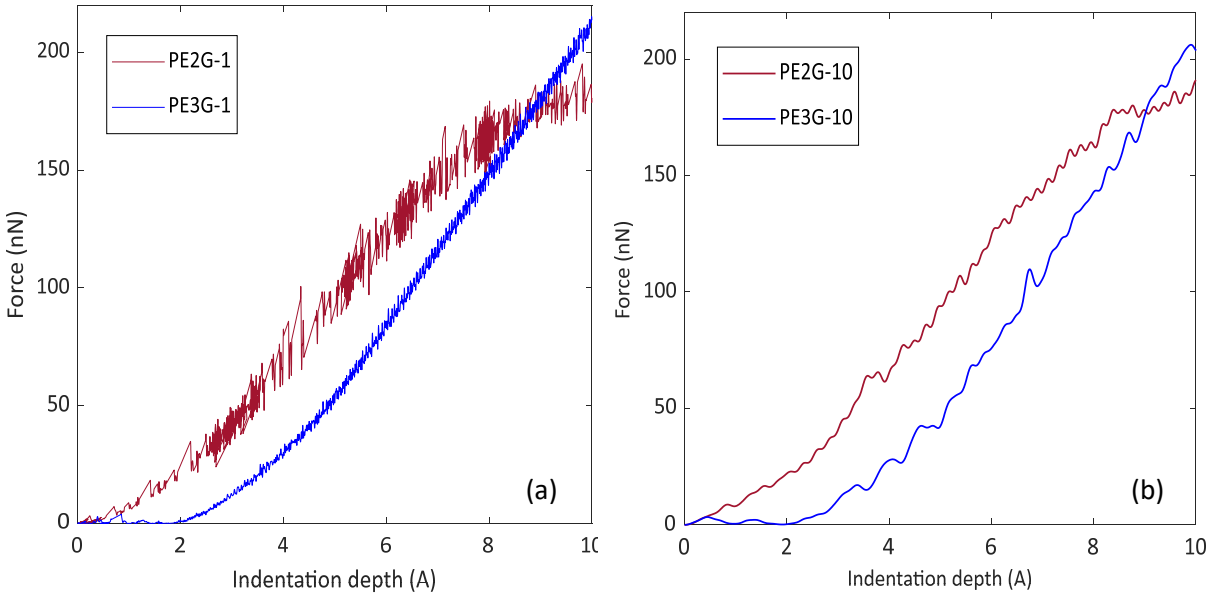

Figure 4.3 Force-indentation depth graphs for PEG, PE2G, and PE3G at (a) 1 $\text{Å}/_{ps}$, and (b) 10 $\text{Å}/_{ps}$

Figure 4.4 plots the interaction energy between graphene and polymer in PE2G and PE3G. As can be seen, the interaction energy between graphene and polymer matrix is larger in PE2G than that in PE3G. This could be responsible for the larger indentation force in PE2G at a displacement less than 8 Å. Our results in figure 4.4 are also consistent with the study of Alian et al., [101] where increment in interaction energy lead to larger indentation forces in PE/G nanocomposites. However, we also notice that PE3G has a larger indentation force at a displacement larger than 9 Å. It is thus of interest to take a look at the corresponding stress distribution.

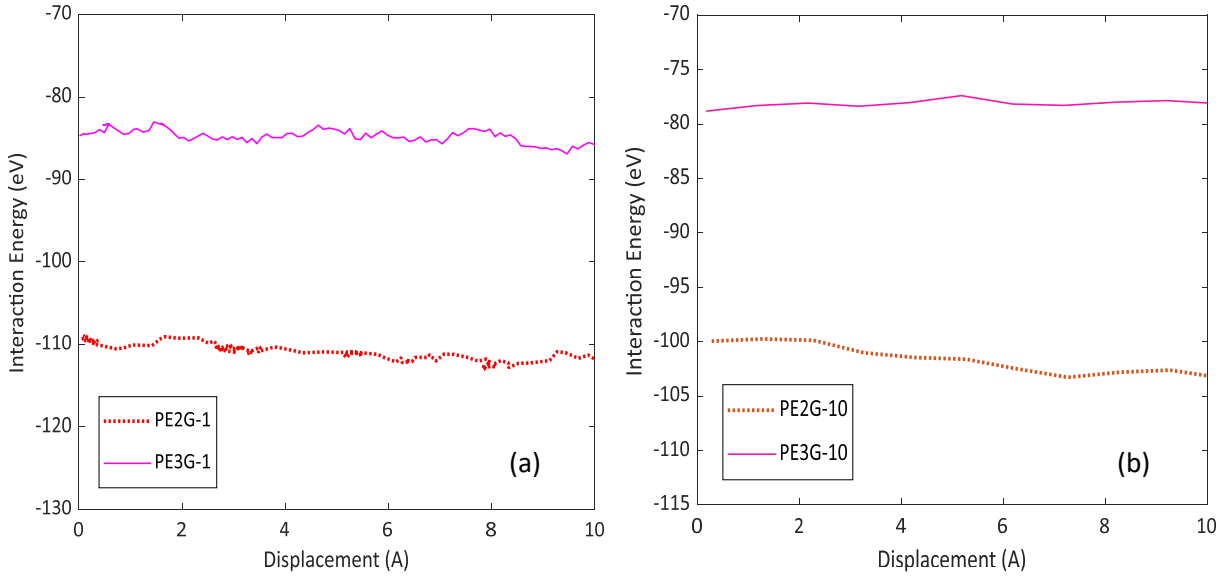

Figure 4.4 Indentation energy-displacement graphs for PEG, PE2G, and PE3G at (a) 1 $\text{Å}/_{ps}$, and (b) 10 $\text{Å}/_{ps}$

Figure 4.5 shows the shear stress distribution at the cross sections of PE2G and PE3G composites. All stress distributions are obtained at an indentation depth of 10 Å. As can be seen in figure 4.5, the stress distributions are more or less uniform in all samples, and the maximum stress in PE3G is larger than that in PE2G. These stress distributions are consistent with the force-displacement plots in figure 4.3, considering that at an indentation depth of 10 angstroms, PE3G samples have a larger indentation force than PE2G at both speeds. At this indentation depth, both polymer and graphene are influenced by the indenter. Thus, samples with more layers of graphene would demand larger indentation forces, considering the reinforcement role of graphene. Indeed, in PE3G, which has a 3-layer graphene, the stress and indentation force is larger than PE2G that has a 2-layer graphene. According to the work of Hossain et al. [19], the number of polymer chains have negligible impact on the maximum force, and thus the

maximum stress. The observation here agrees with Hossain et al., [19] since graphene is responsible for the maximum stress/indentation force at a larger indentation depth (10 Å in figure 4.5). However, at a smaller indentation depth, where the indenter has not contacted the graphene yet, polymers would be responsible for resisting the indenter, leading to larger indentation forces in PE2G than those in PE3G (see figure 4.3). This is due to that PE2G has more polymer chains than PE3G (see table 4.1). It is also noted at comparing the two indenter speeds, PE2G has a slightly larger shear stress at 10 $\text{Å}/_{ps}$, and the opposite is observed for PE3G.

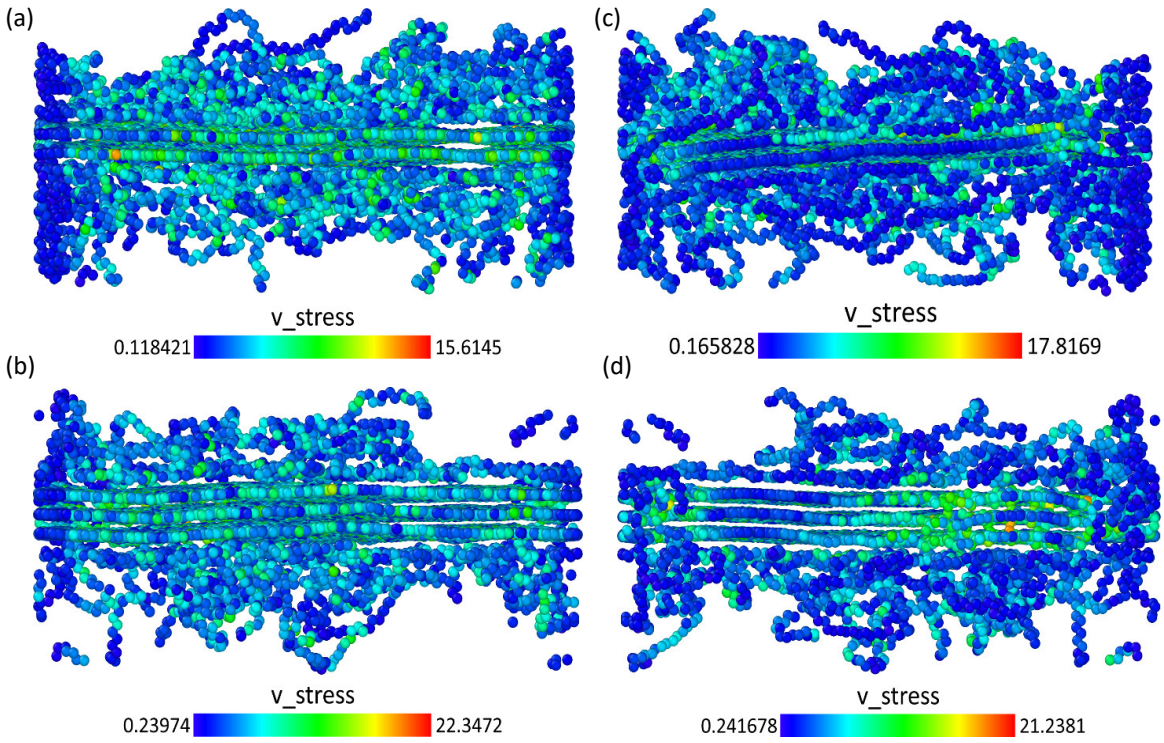

Figure 4.5 Stress distribution along a) PE2G-1, b) PE3G-1, c) PE2G-10, d) PE3G-10

The corresponding shear strain distribution at an indentation depth of 10 Å was plotted in figure 4.6 for the two indentation speeds (1 and 10 $\text{Å}/_{ps}$). For all samples, PE shows relatively larger strain compared to graphene, which can be attributed to the

smaller modulus of PE than that of graphene [1, 102]. Furthermore, comparing PE3G with PE2G, the maximum strain is smaller in PE3G than that of PE2G. This, again, is due to the presence of 3-layer graphene in PE3G, which can provide more resistance to the indentation. At a higher indenter speed (10 $\text{Å}/_{ps}$), the shear strains in both PE2G and PE3G are lower than those at a lower indenter speed (1 $\text{Å}/_{ps}$). This might be attributed to that at a higher indenter speed, there is no sufficient time for the samples, especially the long polymer chains, to response, leading to a smaller shear strain [19]. It needs to be pointed out that due to its high moduli, graphene, while having a smaller strain, can still have a larger stress, and thus demand larger indentation forces. This is, while shear strain is smaller in PE3G, the corresponding stress can be larger than that of PE2G.

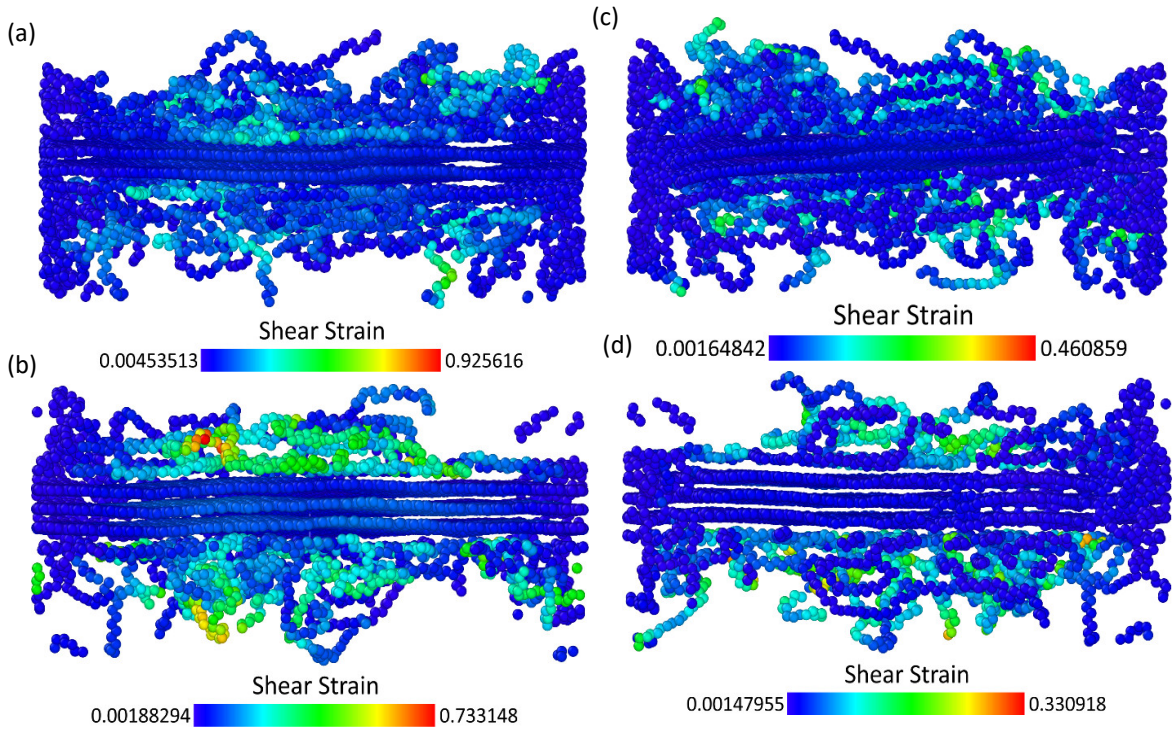

Figure 4.6 Shear strain distribution along a) PE2G-1, b) PE3G-1, c) PE2G-10,d) PE3G-10

4.5 Conclusion

This chapter first investigated the tensile responses of PE chains to validate the model construction and force field. The stress-strain relationships obtained are consistent with literature works. Thus, the same model and force field was used for PE/G composites. Nanoindentation was carried out at two speeds, 1 and 10 $\mathrm{\AA}/_{ps}$. It was found that at these two speeds, the indentation force of PE3G was lower than that of PE2G at a smaller indentation depth. With further increasing indentation depth, the indentation force in PE3G surpass that in PE2G. This is due to the reason that at a larger indentation depth, graphene is responsible for resisting indentation, confirmed by the stress and strain distribution. At both speeds, the maximum stress in PE3G is larger than that in PE2G, while the maximum strain in PE3G is smaller than that in PE2G. The underlying reason is that compared to 2-layer graphene, 3-layer graphene can provide more resistance to the indentation. Furthermore, for the same sample, the maximum strain at 10 $\mathrm{\AA}/_{ps}$ is smaller than that at 1 $\mathrm{\AA}/_{ps}$. This might be attributed to that at a higher indenter speed, there is no sufficient time for the samples to response, leading to a smaller strain. The results achieved in this part can help to understand the reinforcing role of graphene at different stages of deformations.

Chapter 5. Conclusion and Future Works

5.1 Major Conclusions

This thesis adopts MD techniques to probe the mechanical responses of graphene and graphene-reinforced polymer composites. MD simulations are chosen here given that they are ideally suited for providing atomistic details.

A series of MD simulations was first performed to reveal the fundamental mechanisms for the effects of the number of layers, as well as non-bonded interactions, on the mechanical properties of multilayer graphene. It was revealed that for graphene samples under tensile stretch, stress-strain relations and Young's moduli were insensitive to both the interlayer interactions and the number of graphene layers. Contrarily, during nanoindentation tests, both the number of layers and the potentials can influence the force-displacement responses and Young's moduli. Specifically, while increasing layer thicknesses and interlayer interactions can both increase indentation forces, an increment in Young's moduli can only be achieved by increasing interlayer interactions. This is, increasing layer thicknesses decreases the Young's moduli. Detailed strain analysis revealed that while the distribution of normal strains is independent of graphene thicknesses and interlayer interactions, the distribution of shear strains exhibits "strain shielding" phenomena that depend on interlayer interactions. To validate our findings, additional simulations were performed on the hybrids of graphene/boron nitride (GBN) sheets. It was found that compared to pristine graphene sheets, the stronger interlayer interactions provided by BNs in the hybrids can indeed help to promote strain shielding, and thus reduce the decrement effects of the number of layers on the Young's modulus.

Following the above, to reveal the reinforcing role of graphene, MD simulations were then performed on PE/G nanocomposites. Molecular models and force fields were first validated by tensile stretch of PE chains. Then, nanoindentation reveals that at a smaller indentation depth, mechanical responses of the layered nanocomposite are dominated by PE chains, while at a larger indentation depth, graphene is more responsible for providing resistances. Therefore, nanocomposites with more polymer chains have larger indentation forces at smaller indentation depths, while those with more layer of graphene have larger indentation forces at larger indentation depth. In addition, at a relatively high indentation speed, there might be insufficient time for the materials to respond, which leads to reduced maximum shear strains compared to those at a relatively low indentation speed.

5.2 Future Works

Based on the work conducted in this thesis, the following directions are proposed for future studies.

First, multilayer graphene might have misalignments among different layers, in addition to the “perfect”, layer-by-layer stacking used in this thesis. Thus, it is of interest to probe the effect of stacking patterns on the mechanical properties of multilayer graphene. Correspondingly, it is worth studying the effect of these stacking patterns on graphene-reinforced polymer composites. Furthermore, hybrids of graphene and boron nitrides can also be explored as reinforcement materials.

Secondly, when probing PE/G composites in this thesis work, classical Dreiding force field is adopted, which allowed us to probe indentation depth up to 10 Å. In future studies, reactive force fields can be adopted for polymers, and thus enable the study of

fracture behaviors. Based on this, covalent bonds can also be included into the study of interfacial interactions between polymer and graphene, in addition to non-boned interactions. Therefore, further insights may be provided into the reinforcing role of graphene.

6. References

1. Papageorgiou DG, Kinloch IA, Young RJ (2017) Mechanical properties of graphene and graphene-based nanocomposites. Prog Mater Sci 90:75–127. https://doi.org/10.1016/j.pmatsci.2017.07.004

2. Wallace PR (1946) The Band Theory of Graphite. Phys Rev J Arch 71:622. https://doi.org/https://doi.org/10.1103/PhysRev.71.622

3. Novoselov KS, Geim AK, Morozov S V., et al (2004) Electric Field Effect in Atomically Thin Carbon Films. 306:666–669. https://doi.org/10.1126/science.1102896

4. Hamzah AA, Selvarajan RS, Majlis BY (2017) Graphene for biomedical applications: A review. Sains Malaysiana 46:1125–1139. https://doi.org/10.17576/jsm-2017-4607-16

5. Shen C, Oyadiji SO (2020) The processing and analysis of graphene and the strength enhancement effect of graphene-based filler materials: A review. Mater. Today Phys. 15:385–388

6. Rahat Rahman M, Rashid MM, Islam MM, Akanda MM (2019) Electrical and Chemical Properties of Graphene over Composite Materials: A Technical Review. Mater Sci Res India 16:142–163. https://doi.org/10.13005/msri/160208

7. Zhong T, Li J, Zhang K (2019) A molecular dynamics study of Young's modulus of multilayer graphene. J Appl Phys 125:175110. https://doi.org/10.1063/1.5091753

8. Mirnezhad M, Ansari R, Seifi M, et al (2012) Mechanical properties of graphene

under molecular hydrogen physisorption : An ab initio study. Solid State Commun 152:842–845. https://doi.org/10.1016/j.ssc.2012.02.021

9. Chandra Y, Adhikari S, Flores EIS, Figiel Ł (2020) Materials Science & Engineering R Advances in finite element modelling of graphene and associated nanostructures. Mater Sci Eng R 140:100544. https://doi.org/10.1016/j.mser.2020.100544

10. Cui T, Mukherjee S, Sudeep PM, et al (2020) Fatigue of graphene. Nat Mater 19:405–411. https://doi.org/10.1038/s41563-019-0586-y

11. Erkelens R Van, Ruitenbeek J Van, Galli F, Aartsma T (2018) Conducting AFM on graphene

12. Aggarwal SL, Sweeting J (1956) POLYETHYLENE: PREPARATION, STRUCTURE, AND PROPERTIES

13. Falin A, Cai Q, Santos EJG, et al (2017) Mechanical properties of atomically thin boron nitride and the role of interlayer interactions. Nat Commun 8:1–9. https://doi.org/10.1038/ncomms15815

14. Banarouei SA, Yu L, Jian C (2021) Stacking nuances modulate the mechanical properties of graphene/SnO2nanocomposites. Nanotechnology 32:. https://doi.org/10.1088/1361-6528/abeb3b

15. Baseden KA, Tye JW (2014) Introduction to density functional theory: Calculations by hand on the helium atom. J Chem Educ 91:2116–2123. https://doi.org/10.1021/ed5004788

16. Bao Q, Yang Z, Lu Z (2020) Molecular dynamics simulation of amorphous polyethylene (PE) under cyclic tensile-compressive loading below the glass transition temperature. Polymer (Guildf) 186:121968. https://doi.org/10.1016/j.polymer.2019.121968

17. Lee C, Wei X, Kysar JW, Hone J (2008) of Monolayer Graphene. Science (80-) 321:385–388

18. Zhang W, Wang Z, Lv S, et al (2021) Molecular simulation of different structure dopamine-modified graphene oxide and its effects on thermal and mechanical properties of the epoxy resin system. Polymer (Guildf) 212:123120. https://doi.org/10.1016/j.polymer.2020.123120

19. Hossain D, Tschopp MA, Ward DK, et al (2010) Molecular dynamics simulations of deformation mechanisms of amorphous polyethylene. Polymer (Guildf) 51:6071–6083. https://doi.org/10.1016/j.polymer.2010.10.009

20. Li Y, Wang S, Wang Q (2017) A molecular dynamics simulation study on enhancement of mechanical and tribological properties of polymer composites by introduction of graphene. Carbon N Y 111:538–545. https://doi.org/10.1016/j.carbon.2016.10.039

21. Chen T, Cheung R (2016) Mechanical properties of graphene. In: Graphene Science Handbook: Mechanical and Chemical Properties. pp 3–15

22. Zandiatashbar A, Lee GH, An SJ, et al (2014) Effect of defects on the intrinsic strength and stiffness of graphene. Nat Commun 5:1–9. https://doi.org/10.1038/ncomms4186

23. Han J, Ryu S, Kim DK, et al (2016) Effect of interlayer sliding on the estimation of elastic modulus of multilayer graphene in nanoindentation simulation. Epl 114:. https://doi.org/10.1209/0295-5075/114/68001

24. Li Y, Zhang W, Guo B, Datta D (2017) Interlayer shear of nanomaterials: Graphene–graphene, boron nitride–boron nitride and graphene–boron nitride. Acta Mech Solida Sin 30:234–240. https://doi.org/10.1016/j.camss.2017.05.002

25. Goda K, Sreekala MS, Malhotra SK, et al (2013) Advances in polymer composites: Biocomposites-state of the art, new challenges, and opportunities. In: Polymer Composites, Biocomposites. pp 1–10

26. Young RJ, Gong L, Kinloch IA, et al (2011) Strain mapping in a graphene monolayer nanocomposite. ACS Nano 5:3079–3084. https://doi.org/10.1021/nn2002079

27. Gong L, Young RJ, Kinloch IA, et al (2012) Optimizing the reinforcement of polymer-based nanocomposites by graphene. ACS Nano 6:2086–2095. https://doi.org/10.1021/nn203917d

28. Liu P, Koman VB, Kozawa D, Strano MS (2019) Materials design for robotic platforms enabling unique mechanisms of projectile protection. In: Robotic Systems and Autonomous Platforms. Elsevier Ltd., pp 493–521

29. Hummers WS, Offeman RE (1958) Preparation of Graphitic Oxide. J Am Chem Soc 80:1339. https://doi.org/10.1021/ja01539a017

30. Du J, Cheng HM (2012) The fabrication, properties, and uses of

graphene/polymer composites. Macromol Chem Phys 213:1060–1077. https://doi.org/10.1002/macp.201200029

31. Ogden RW (1973) Large Deformation Isotropic Elasticity - on the Correlation of Theory and Experiment for Incompressible Rubberlike Solids. Rubber Chem Technol 46:398–416. https://doi.org/10.5254/1.3542910

32. Monji F, Jabbareh MA (2017) CALPHAD : Computer Coupling of Phase Diagrams and Thermodynamic model for prediction of binary alloy nanoparticle phase diagram including size dependent surface tension e ff ect. Calphad 58:1–5. https://doi.org/10.1016/j.calphad.2017.04.003

33. Müller T, Sharma S, Gross EKU, Dewhurst JK (2020) Extending Solid-State Calculations to Ultra-Long-Range Length Scales. Phys Rev Lett 125:256402. https://doi.org/10.1103/PhysRevLett.125.256402

34. Jia W, Wang H, Chen M, et al (2020) Pushing the limit of molecular dynamics with ab initio accuracy to 100 million atoms with machine learning. Int Conf High Perform Comput Networking, Storage Anal SC 2020-Novem: https://doi.org/10.1109/SC41405.2020.00009

35. Liu X, He X, Wang J, et al (2018) An ordinary state-based peridynamic model for the fracture of zigzag graphene sheets. Proc R Soc A Math Phys Eng Sci 474:. https://doi.org/10.1098/rspa.2018.0019

36. Pal, Snehanshu Ray BC (2016) Molecular Dynamics Simulation of Nanostructured Materials: An Understanding of Mechanical Behavior

37. Kukol A (2016) Trying to Understand Waiting for Godot: An Adornian Analysis of Beckett's Signature Work. Humana Press

38. Hollingsworth SA, Dror RO (2018) Molecular Dynamics Simulation for All. Neuron 99:1129–1143. https://doi.org/10.1016/j.neuron.2018.08.011

39. Buehler MJ (2007) Atomistic Modeling of Materials Failure

40. González MA (2011) Force fields and molecular dynamics simulations. 12:169–200. https://doi.org/http://dx.doi.org/10.1051/sfn/201112009

41. Senftle TP, Hong S, Islam MM, et al (2016) The ReaxFF reactive force-field: Development, applications and future directions. npj Comput Mater 2:. https://doi.org/10.1038/npjcompumats.2015.11

42. Tersoff J (1989) Modeling solid-state chemistry: Interatomic potentials for multicomponent systems. Phys Rev B 39:5566–5568. https://doi.org/10.1103/PhysRevB.39.5566

43. Plimption S (1994) Fast Parallel Algorithms for Short-Range Molecular Dynamics. J Comput Phys 1–19. https://doi.org/10.1039/c7sm02429k

44. Abraham MJ, Murtola T, Schulz R, et al (2015) Gromacs: High performance molecular simulations through multi-level parallelism from laptops to supercomputers. SoftwareX 1–2:19–25. https://doi.org/10.1016/j.softx.2015.06.001

45. Andoh CN, Ayensu Gyeabour I A, Banini GK (2020) MOLECULAR DYNAMICS SIMULATION OF MECHANICAL DEFORMATION OF AUSTENITIC STAINLESS

STEELS (Fe-Ni-Cr ALLOYS) AT SUPERCRITICAL WATER CONDITIONS. J Appl Sci Technol 22:01–13

46. Nieto A, Bisht A, Lahiri D, et al (2017) Graphene reinforced metal and ceramic matrix composites: a review. Int Mater Rev 62:241–302. https://doi.org/10.1080/09506608.2016.1219481

47. Mittal G, Dhand V, Rhee KY, et al (2015) A review on carbon nanotubes and graphene as fillers in reinforced polymer nanocomposites. J Ind Eng Chem 21:11–25. https://doi.org/10.1016/j.jiec.2014.03.022

48. Patil SP (2019) Nanoindentation of graphene-reinforced silica aerogel: A molecular dynamics study. Molecules 24:1336–1348. https://doi.org/10.3390/molecules24071336

49. Moeini M, Barbaz Isfahani R, Saber-Samandari S, Aghdam MM (2020) Molecular dynamics simulations of the effect of temperature and strain rate on mechanical properties of graphene–epoxy nanocomposites. Mol Simul 46:476–486. https://doi.org/10.1080/08927022.2020.1729983

50. Najafi F, Wang G, Mukherjee S, et al (2020) Toughening of graphene-based polymer nanocomposites via tuning chemical functionalization. Compos Sci Technol 194:108140. https://doi.org/10.1016/j.compscitech.2020.108140

51. Li M, Zhou H, Zhang Y, et al (2017) The effect of defects on the interfacial mechanical properties of graphene/epoxy composites. RSC Adv 7:46101–46108. https://doi.org/10.1039/c7ra08243f

52. Li J, Zhao J, Ren P, et al (2019) Effects of temperature, strain rate and molecule length on the deformation of graphene/polyethylene composites: A molecular dynamics simulation. Chem Phys Lett 726:39–45. https://doi.org/10.1016/j.cplett.2019.04.037

53. Georgantzinos SK, Giannopoulos GI, Anifantis NK (2010) Numerical investigation of elastic mechanical properties of graphene structures. Mater Des 31:4646–4654. https://doi.org/10.1016/j.matdes.2010.05.036

54. Dewapriya MAN, Srikantha Phani A, Rajapakse RKND (2013) Influence of temperature and free edges on the mechanical properties of graphene. Model Simul Mater Sci Eng 21:065017. https://doi.org/10.1088/0965-0393/21/6/065017

55. Fan N, Ren Z, Jing G, et al (2017) Numerical investigation of the fracture mechanism of defective graphene sheets. Materials (Basel) 10:164–176. https://doi.org/10.3390/ma10020164

56. Damasceno DA, Rajapakse RKNDN, Mesquita E (2020) Atomistic modelling of size-dependent mechanical properties and fracture of pristine and defective cove-edged graphene nanoribbons. Nanomaterials 10:1–15. https://doi.org/10.3390/nano10071422

57. Zhang YY, Gu YT (2013) Mechanical properties of graphene: Effects of layer number, temperature and isotope. Comput Mater Sci 71:197–200. https://doi.org/10.1016/j.commatsci.2013.01.032

58. Hosseini Kordkheili SA, Moshrefzadeh-Sani H (2013) Mechanical properties of double-layered graphene sheets. Comput Mater Sci 69:335–343.

https://doi.org/10.1016/j.commatsci.2012.11.027

59. Zhang Y, Pan C (2012) Measurements of mechanical properties and number of layers of graphene from nano-indentation. Diam Relat Mater 24:1–5. https://doi.org/10.1016/j.diamond.2012.01.033

60. Neek-Amal M, Peeters FM (2010) Nanoindentation of a circular sheet of bilayer graphene. Phys Rev B - Condens Matter Mater Phys 81:1–6. https://doi.org/10.1103/PhysRevB.81.235421

61. Muniz AR, Machado AS, Maroudas D (2015) Mechanical behavior of interlayer-bonded nanostructures obtained from bilayer graphene. Carbon N Y 81:663–677. https://doi.org/10.1016/j.carbon.2014.10.003

62. Zhang YY, Wang CM, Cheng Y, Xiang Y (2011) Mechanical properties of bilayer graphene sheets coupled by sp3 bonding. Carbon N Y 49:4511–4517. https://doi.org/10.1016/j.carbon.2011.06.058

63. Machado AS, Maroudas D, Muniz AR (2013) Tunable mechanical properties of diamond superlattices generated by interlayer bonding in twisted bilayer graphene. Appl Phys Lett 103:013113. https://doi.org/10.1063/1.4813271

64. Kumar S, Parks DM (2015) Strain shielding from mechanically activated covalent bond formation during nanoindentation of graphene delays the onset of failure. Nano Lett 15:1503–1510. https://doi.org/10.1021/nl503641c

65. Hosseini E, Zakertabrizi M, Habibnejad Korayem A, Shahsavari R (2019) Tunable, Multifunctional Ceramic Composites via Intercalation of Fused Graphene

Boron Nitride Nanosheets. ACS Appl Mater Interfaces 11:8635–8644. https://doi.org/10.1021/acsami.8b19409

66. Ding N, Chen X, Wu CML (2016) Mechanical properties and failure behaviors of the interface of hybrid graphene/hexagonal boron nitride sheets. Sci Rep 6:1–9. https://doi.org/10.1038/srep31499

67. Li P, Cao K, Jiang C, et al (2019) In situ tensile fracturing of multilayer graphene nanosheets for their in-plane mechanical properties. Nanotechnology 30:. https://doi.org/10.1088/1361-6528/ab3cd3

68. Zhang P, Ma L, Fan F, et al (2014) Fracture toughness of graphene. Nat Commun 5:1–7. https://doi.org/10.1038/ncomms4782

69. Wei X, Xiao S, Li F, et al (2015) Comparative fracture toughness of multilayer graphenes and boronitrenes. Nano Lett 15:689–694. https://doi.org/10.1021/nl5042066

70. Jang B, Mag-isa AE, Kim JH, et al (2017) Uniaxial fracture test of freestanding pristine graphene using in situ tensile tester under scanning electron microscope. Extrem Mech Lett 14:10–15. https://doi.org/10.1016/j.eml.2016.11.001

71. Han J, Ryu S, Kim DK, et al (2016) Effect of interlayer sliding on the estimation of elastic modulus of multilayer graphene in nanoindentation simulation. EPL 114:. https://doi.org/10.1209/0295-5075/114/68001

72. Chen X, Yi C, Ke C (2015) Bending stiffness and interlayer shear modulus of few-layer graphene. Appl Phys Lett 106:. https://doi.org/10.1063/1.4915075

73. Borodich FM, Galanov BA (2016) Contact probing of stretched membranes and adhesive interactions: Graphene and other two-dimensional materials. Proc R Soc A Math Phys Eng Sci 472:20160550. https://doi.org/10.1098/rspa.2016.0550

74. Niu T, Cao G, Xiong C (2018) Indentation behavior of the stiffest membrane mounted on a very compliant substrate: Graphene on PDMS. Int J Solids Struct 132–133:1–8. https://doi.org/10.1016/j.ijsolstr.2017.05.038

75. Cao C, Daly M, Singh CV, et al (2015) High strength measurement of monolayer graphene oxide. Carbon N Y 81:497–504. https://doi.org/10.1016/j.carbon.2014.09.082

76. Chernozatonskii LA, Demin VA, Artyukh AA (2016) Formation, structure, and properties of “welded” h-BN/graphene compounds. JETP Lett 104:43–48. https://doi.org/10.1134/S0021364016130063

77. Stuart SJ, Tutein AB, Harrison JA (2000) A reactive potential for hydrocarbons with intermolecular interactions. J Chem Phys 112:6472–6486. https://doi.org/10.1063/1.481208

78. Dewapriya MAN, Meguid SA (2019) Comprehensive molecular dynamics studies of the ballistic resistance of multilayer graphene-polymer composite. Comput Mater Sci 170:109171. https://doi.org/10.1016/j.commatsci.2019.109171

79. Giannopoulos GI, Liosatos IA, Moukanidis AK (2011) Parametric study of elastic mechanical properties of graphene nanoribbons by a new structural mechanics approach. Phys E Low-Dimensional Syst Nanostructures 44:124–134. https://doi.org/10.1016/j.physe.2011.08.001

80. Norouzi S, Fakhrabadi MMS (2019) Nanomechanical properties of single- and double-layer graphene spirals: a molecular dynamics simulation. Appl Phys A Mater Sci Process 125:1–11. https://doi.org/10.1007/s00339-019-2623-8

81. Wang X, Ramírez-Hinestrosa S, Dobnikar J, Frenkel D (2020) The Lennard-Jones potential: When (not) to use it. Phys Chem Chem Phys 22:10624–10633. https://doi.org/10.1039/c9cp05445f

82. Lee JH (2006) A study on a boron-nitride nanotube as a gigahertz oscillator. J Korean Phys Soc 49:172–176. https://doi.org/https://inis.iaea.org/search/search.aspx?orig_q=RN:43010880

83. Fan Y, Cao P (2019) Long Time-Scale Atomistic Modeling and Simulation of Deformation and Flow in Solids. In: Handbook of Materials Modeling. Springer International Publishing, Cham, pp 1–27

84. G. Hoover W (1985) Canonical dynamics: Equilibrium phase-space distributions. Phys Rev A 31:1695–1697. https://doi.org/10.1103/PhysRevA.31.1695

85. Hoover WG (1986) Constant-pressure equations of motion. Phys Rev A 34:2499–2500. https://doi.org/10.1103/PhysRevA.34.2499

86. Stukowski A (2010) Visualization and analysis of atomistic simulation data with OVITO-the Open Visualization Tool. Model Simul Mater Sci Eng 18:015012. https://doi.org/10.1088/0965-0393/18/1/015012

87. Tan X, Wu J, Zhang K, et al (2013) Nanoindentation models and Young's modulus of monolayer graphene: A molecular dynamics study. Appl Phys Lett

102:071908. https://doi.org/10.1063/1.4793191

88. Jin C (2017) Comment on “Nanoindentation models and Young’s modulus of monolayer graphene: A molecular dynamics study.” Appl Phys Lett 110:176101. https://doi.org/10.1063/1.4982226

89. Begley MR, Mackin TJ (2004) Spherical indentation of freestanding circular thin films in the membrane regime. J Mech Phys Solids 52:2005–2023. https://doi.org/10.1016/j.jmps.2004.03.002

90. Liu A, Peng Q (2018) A molecular dynamics study of the mechanical properties of twisted bilayer graphene. Micromachines 9:1–11. https://doi.org/10.3390/mi9090440

91. Rahman R, Foster JT (2014) Deformation mechanism of graphene in amorphous polyethylene: A molecular dynamics based study. Comput Mater Sci 87:232–240. https://doi.org/10.1016/j.commatsci.2014.02.023

92. Alasvand Zarasvand K, Golestanian H (2017) Investigating the effects of number and distribution of GNP layers on graphene reinforced polymer properties: Physical, numerical and micromechanical methods. Compos Sci Technol 139:117–126. https://doi.org/10.1016/j.compscitech.2016.12.024

93. Degirmenci U, Erturk AS, Yurtalan MB, Kirca M (2021) Tensile behavior of nanoporous polyethylene reinforced with carbon-based nanostructures. Comput Mater Sci 186:109971. https://doi.org/10.1016/j.commatsci.2020.109971

94. Liu J, Shen J, Zheng Z, et al (2015) Revealing the toughening mechanism of

graphene-polymer nanocomposite through molecular dynamics simulation. Nanotechnology 26:. https://doi.org/10.1088/0957-4484/26/29/291003

95. Rissanou AN, Power AJ, Harmandaris V (2015) Structural and dynamical properties of polyethylene/graphene nanocomposites through molecular dynamics simulations. Polymers (Basel) 7:390–417. https://doi.org/10.3390/polym7030390

96. Verma A, Parashar A, Packirisamy M (2019) Effect of grain boundaries on the interfacial behaviour of graphene-polyethylene nanocomposite. Appl Surf Sci 470:1085–1092. https://doi.org/10.1016/j.apsusc.2018.11.218

97. Liu F, Hu N, Zhang J, et al (2016) The interfacial mechanical properties of functionalized graphene–polymer nanocomposites. 66658–66664. https://doi.org/10.1039/c6ra09292f

98. Truong GT, Van Tran H, Choi KK (2020) Investigation on mode i fracture toughness of woven carbon fiber-reinforced polymer composites incorporating nanomaterials. Polymers (Basel) 12:1–23. https://doi.org/10.3390/polym12112512

99. Stuart SJ, Tutein AB, Harrison JA (2000) A reactive potential for hydrocarbons with intermolecular interactions. J Chem Phys 112:6472–6486. https://doi.org/10.1063/1.481208

100. Chen S, Liu Q, Gorbatikh L, Seveno D (2021) Does Thermal Percolation Exist in Graphene-Reinforced Polymer Composites? A Molecular Dynamics Answer. J Phys Chem C 125:1018–1028. https://doi.org/10.1021/acs.jpcc.0c09249

101. Alian AR, Dewapriya MAN, Meguid SA (2017) Molecular dynamics study of the

reinforcement effect of graphene in multilayered polymer nanocomposites. Mater Des 124:47–57. https://doi.org/10.1016/j.matdes.2017.03.052

102. Hageman JCL, Meier RJ, Heinemann M, De Groot RA (1997) Young modulus of crystalline polyethylene from ab initio molecular dynamics. Macromolecules 30:5953–5957. https://doi.org/10.1021/ma9703721